Article

The contribution of rock strength to soil production

https://doi.org/10.1038/s41586-025-09751-z

Received: 30 August 2024

Accepted: 14 October 2025

Published online: 12 November 2025

Check for updates

Emily C. Geyman[1]✉, David A. Paige[2] & Michael P. Lamb[1]

It has long been proposed[1], and then observed[2,3], that faster rates of soil production occur beneath thinner soils. It remains uncertain, however, whether soil thickness is the driving variable regulating production from the top-down[2–6], or whether soil thickness is simply responding to changes in bedrock weathering controlled from the bottom-up[7,8]. Answering this question is difficult because the feedbacks between soil production and soil erosion, the processes that jointly govern soil thickness[2,9,10], respond to perturbations on timescales of thousands to millions of years[11,12], timescales that are too long for scientists to observe directly. Here we leverage a space-for-time substitution at a transient mountain range along the San Andreas Fault[13–15], where the remarkable tectonic setting allows for independent quantification of uplift, soil production and erosion. We show that, following a pulse of tectonic uplift, the conversion of rock to soil accelerates before the overlying soils thin, but at the same time that topographic stresses increase[7] and the rock weakens[16]. This observation challenges the long-standing assumption that soil production rates are controlled predominantly by soil thickness[1,2], and instead lends evidence for a bottom-up, rock strength control on soil production.

Soil production is the process by which rock is broken down into the small, mobile particles that comprise soil. Despite its simple definition, this transformation represents a key rate-limiting step that controls factors as wide ranging as the height of mountains and the shape of landscapes[17], the pace of the silicate weathering feedback (Earth's key mechanism for CO_2 drawdown)[3,18] and the sustainability of modern agriculture[19]. However, we still lack an understanding of what controls the pace of this rock-to-soil transformation[17,20,21]. The competing rates of soil production (P) and soil erosion (E) determine the thickness (H) of the soil layer draping Earth's hillslopes (Fig. 1a):

$$\frac{\mathrm{d}H}{\mathrm{d}t} = \left(\frac{\rho_\mathrm{r}}{\rho_\mathrm{s}}\right)P - E \quad (1)$$

where ρ_r and ρ_s are the bulk densities of rock and soil, respectively. The fact that measured denudation rates span about four orders of magnitude across Earth[22], yet upland soils are nearly always between 0.1 m and 2.0 m deep[19,21], implies that there is a strong feedback keeping P and E in balance. The need for a mechanistic feedback linking soil production and erosion has been recognized for more than a century[1,2,9,10,23,24], and typically it has been framed in terms of a relationship between soil production and soil thickness. If soil production is a monotonically decreasing function of soil thickness (Fig. 1b), then a stable landscape can emerge in which stochastic perturbations to the local soil thickness trigger compensating changes in P that allow the perturbations to decay back to a stable steady state.

The relationship shown in Fig. 1b is supported by three decades of observations[2,3,17]. Yet, this correlation between soil thickness and soil production does not necessarily reveal the underlying mechanism driving soil production. Many have suggested that thinner soils allow enhanced chemical weathering[4,12,20,21,25] and biological disturbance[5,26] at the boundary between the soil and the weathered bedrock (saprolite), implying that soil thickness exerts a top-down control on soil production (Fig. 1b,c). According to this scenario, an increase in the rate of tectonic uplift triggers an increase in the soil erosion rate, which thins soils and enhances weathering at the soil–saprolite boundary[4,5,12,20,21,25,26], causing an increase in the rate of soil production (Fig. 1c). An alternative explanation is that soil thickness is a response variable rather than a driving one. Recent observations of rock strength[16] have shown that hillslopes with rapid soil production are underlain by weaker saprolite (Fig. 1d). This observation is consistent with a scenario in which increased tectonic uplift and channel incision leads to a reduction in rock strength (due to tectonic and topographic stresses[7,27] and/or subsurface chemical weathering[8]), which increases soil production (Fig. 1e). A diagnostic fingerprint differentiating the top-down and bottom-up scenarios is whether, following a pulse of tectonic uplift, the soil thickness change leads or lags the changes in rock strength and soil production. In other words, a distinguishing signal is whether the hysteresis in soil thickness compared with rock strength (h compared with S) proceeds anticlockwise or clockwise (Fig. 1).

A rare window into landscape transience during uplift

Since the hysteresis loops in Fig. 1 unfold over timescales of approximately 10^3–10^5 years, we cannot observe the evolution of any individual

[1]Division of Geological and Planetary Sciences, California Institute of Technology, Pasadena, CA, USA. [2]Department of Earth, Planetary and Space Sciences, University of California, Los Angeles, Los Angeles, CA, USA. ✉e-mail: egeyman@caltech.edu

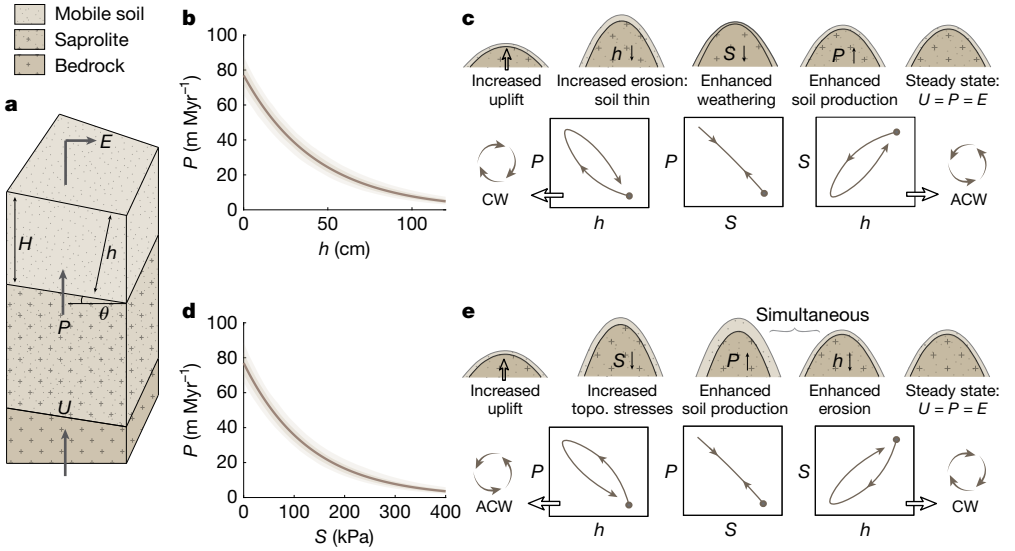

Fig. 1 | Theoretical models for how hillslopes respond to uplift. a, Mass conservation links tectonic uplift (U), soil production (P) and erosion (E) (ref. 10). **b**, The canonical soil production function[2] postulates that P is a negative-exponential function of soil thickness (h). **d**, A complement to **b** is the observation[16] that P is inversely related to saprolite strength (S). **c**, Top-down scenario. An increase in tectonic uplift triggers an increase in erosion. As a result, the soil layer thins, which enhances weathering at the soil–saprolite boundary, causing an increase in soil production. **e**, Bottom-up scenario. Tectonic uplift leads to increased topographic relief, because bedrock channel incision proceeds before the pulse of uplift is communicated to the hilltops[13,15]. The increased relief promotes higher topographic stresses[7,27], which weaken the saprolite and elevate soil production rates. The steeper hillslopes also lead to faster hillslope sediment transport[9,10,23,24], and specifically to greater divergence of the sediment transport (soil erosion[9,10,23,24]) near the hilltops[15]. Thus, uplift, soil production and erosion come into balance, and a new steady state is achieved. Two diagnostic fingerprints differentiating the top-down (**c**) and bottom-up (**e**) scenarios are the directions of the h–P and h–S hysteresis loops. CW, clockwise; ACW, anticlockwise.

hillslope over sufficient time to witness the geomorphic response to uplift[11,12]. However, a small mountain range along the San Andreas Fault (SAF) in California (Fig. 2) provides an opportunity to use a space-for-time substitution[13,14] to observe the causes and consequences of geomorphic change. At the Dragon's Back Pressure Ridge (DBPR), a subsurface offset in the SAF forces the Pacific Plate, which is advected northward at a rate[28] of about 33 mm yr^{-1}, to be pushed upwards, forming a pressure ridge with around 100 m of topographic relief[13,14] (Fig. 2a,b). The Pacific Plate then continues northward like a conveyer belt past this structural knuckle[13,14], and erosion begins to outpace uplift, allowing the steep hillslopes to decay back towards the valley floor (Fig. 2). The DBPR has been used previously[13,15] to demonstrate how topographic form, captured through parameters such as channel steepness[13] and hilltop curvature[15], record the transient perturbations associated with the uplift and erosion of a landscape. Here, we build on previous work by using independent observations to quantify soil production (P), soil erosion (E), soil thickness (h), and rock strength (S) across the DBPR, and thereby test the models shown in Fig. 1. These observations of transient behaviour across space allow us to pinpoint what geomorphic parameters drive changes to soil production and what parameters respond to these changes.

The mass balance of soil production

Using mass conservation, the rate of soil production can be expressed as

$$P = U - \frac{\rho_s}{\rho_r}\left(\frac{dz}{dt} - \frac{dH}{dt}\right) \quad (2)$$

where U (L T^{-1}) is the bedrock uplift rate, $\frac{dz}{dt}$ (L T^{-1}) is the rate of surface elevation change, and $\frac{dH}{dt}$ (L T^{-1}) is the rate of soil thickness change[10] (Methods). Classically, the soil production rate has been estimated using the concentration of cosmogenic nuclides (for example, ^{10}Be) in the saprolite[2,3] (Fig. 1a). However, this method requires a crucial steady-state assumption[2,29], which is probably violated in real landscapes susceptible to episodic erosion[29]. Recent modelling suggests that the exponential soil production function shown in Fig. 1 (ref. 2) could be a methodological artefact of the assumptions required to convert ^{10}Be concentrations to soil production rates[29]. However, an alternative way to quantify P is to generate independent measurements of U, $\frac{dH}{dt}$ and $\frac{dz}{dt}$, and then apply mass conservation (equation (2)). The DBPR is a rare field site where it is possible to do so (Fig. 2).

Independent constraints on uplift, soil thickness and erosion

Reconstructing uplift from stratigraphic constraints

Progressive uplift and erosion at DBPR exposes deeper and deeper sedimentary layers of the initially flat-lying Paso Robles Formation[13,14] (Fig. 2c). Before uplift begins at the structural knuckle, the topmost grey member of the Paso Robles Formation is exposed at the surface (Fig. 2e, A → A′). After the full pulse of uplift has occurred but before the hillslopes have had enough time to undergo substantial erosion[13,15], the middle tan member is exposed at the surface (Fig. 2e, B → B′). Finally, at the end of DBPR, where 80 kyr of erosion has denuded the hillslopes, the lowest pink member is exposed at the surface (Fig. 2e, C → C′). By pairing the geological map with a lidar digital elevation model (Fig. 2b,c), we can track the elevations of the stratigraphic contacts and invert for the spatial pattern of uplift (Fig. 2g,h). This methodology was initially put forth in the pioneering work of ref. 13. We adopt their same approach. However, note in equation (2) that any uncertainties in U are mapped to uncertainties in P. Thus, for our application, we need a quantitative inversion that produces the most likely uplift history while incorporating uncertainties from the geological constraints. Specifically, three variables affect how uplift translates to the observed positions and elevations of the geologic contacts shown in Fig. 2c: (1) the thickness of the tan member of the Paso Robles Formation; (2) the initial elevation of the tan–grey contact; and (3) the position of the inflection in the monoclinal folding

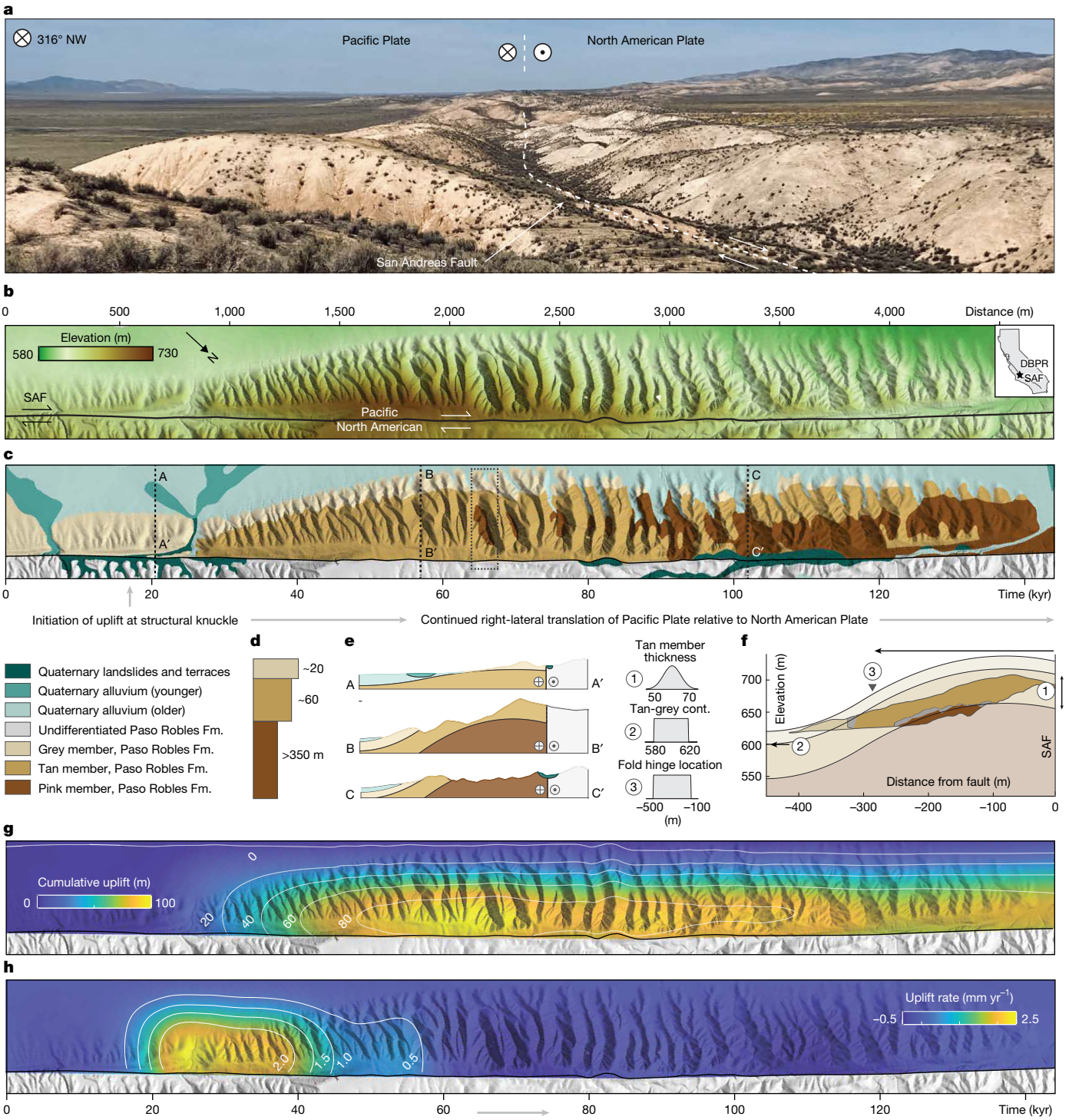

Fig. 2 | Reconstructing uplift and erosion at the DBPR (35.10° N, 119.63° W). **a**,**b**, Right-lateral motion along the SAF moves the Pacific Plate past the North American Plate at a rate of about 33 mm yr^{-1} (ref. 28). Thus, the 4.5 km of translation along the pressure ridge (**b**) corresponds to about 140 kyr. **c**,**d**, Geologic mapping[13,14] at 1:8,000 scale shows the progressive uplift and exhumation of the Plio-Pleistocene Paso Robles Formation. **e**, Geological cross-sections at A → A′, B → B′ and C → C′. We use an MCMC inversion to quantify the total rock uplift along the pressure ridge using the topographic and geological data in **b** and **c**. **f**, Our uplift model requires constraining three parameters: (1) the stratigraphic thickness of the tan member of the Paso Robles Formation (constrained from mapped geological contacts[13,14] to be in the range 50–70 m); (2) the initial elevation of the contact between the tan and grey members (constrained from paired map-view geological contacts and digital elevation data to be in the range 580–620 m above sea level); and (3) the horizontal position (distance from the SAF) of the fold inflection (constrained from bedding plane dip observations[14] to be between 450 m and 150 m away from the fault). **g**,**h**, The MCMC inversion uses lidar elevation data at the positions of the mapped stratigraphic contacts (**b** and **c**) to produce estimates of cumulative uplift (**g**). By taking the along-strike spatial derivative of the cumulative uplift and translating space to time using long-term fault slip rates[28], we resolve the spatial pattern of uplift rates (U) (**h**).

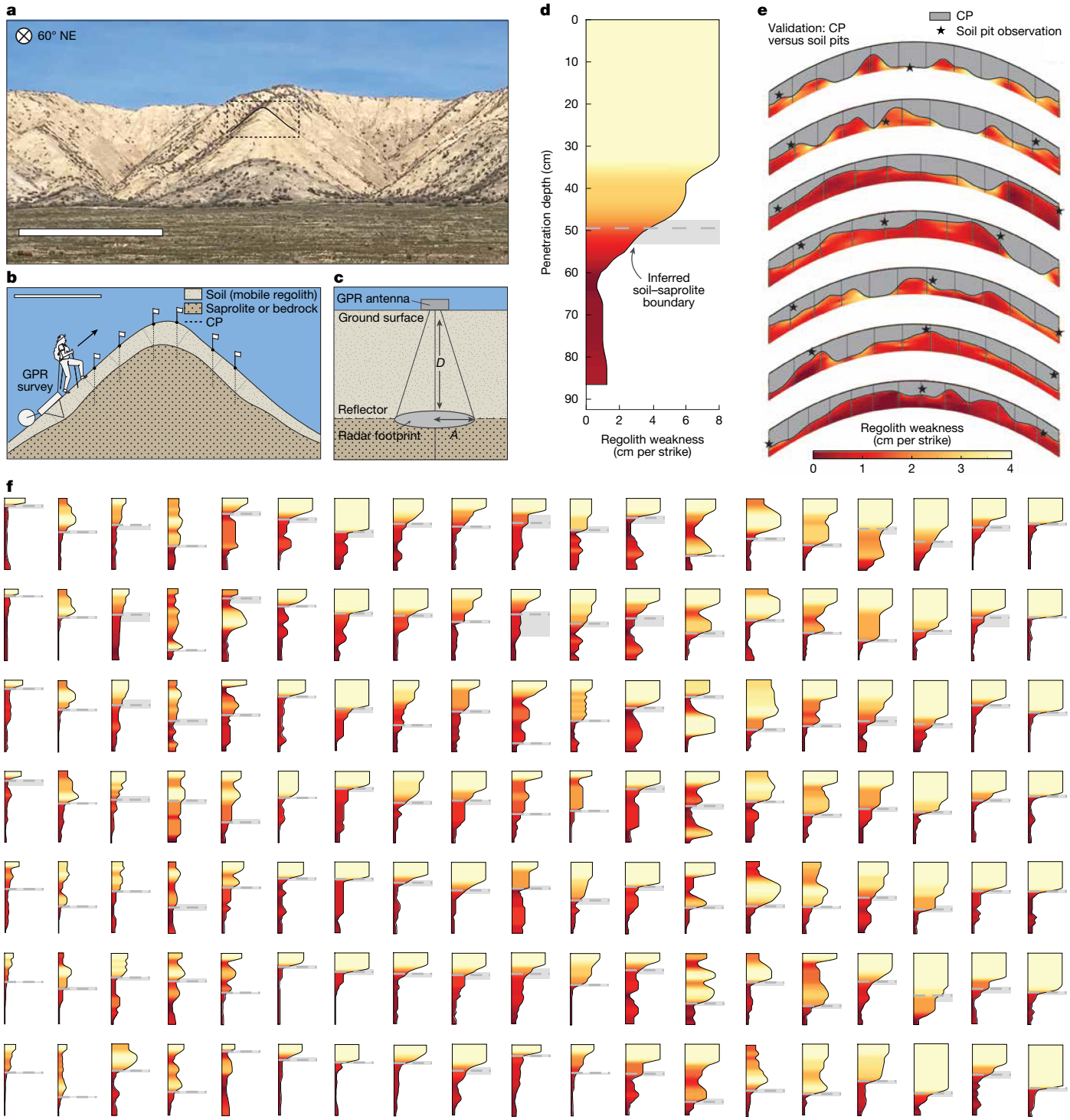

Fig. 3 | Field observations of soil thickness and saprolite strength. a–c, We use GPR to image the soil–saprolite boundary. In total, we surveyed 19 km of ridgelines along DBPR (Extended Data Fig. 6b). At $n = 21$ locations, we analysed ridgetop cross-sections (**a**) with co-located cone penetrometer profiles and GPR surveys (**b**). The GPR is used to image the soil–saprolite boundary (**c**). **d**, The hand-driven dynamic cone penetrometer (see Extended Data Fig. 7a for a diagram) enables the quantification of regolith (soil and saprolite) weakness as a function of depth. **e**, We use co-located soil pits and cone penetrometer profiles to validate the hypothesis that the reduction of regolith weakness at depth is associated with the transition from soil to saprolite. **f**, Example motifs of the near-surface regolith strength quantified with the cone penetrometer. Each profile in **f** has the same axes as in **d**.

geometry shown in Fig. 2f, which is constrained by bedding plane measurements[14] (Methods). We design a Markov Chain Monte Carlo (MCMC) inversion to explore the full plausible range of values for these parameters and constrain the most likely tectonic uplift history at DBPR (Fig. 2g,h). The result is a spatially explicit map of U with associated uncertainties (Fig. 2h).

Measuring soil thickness

We use a combination of hand-dug soil pits, cone penetrometer measurements and ground-penetrating radar (GPR) to quantify soil thickness along the convex hilltops at DBPR (Fig. 3a–c). The GPR survey covers 19 km of ridgelines. To estimate $\frac{dH}{dt}$ (equation (2)), we compare

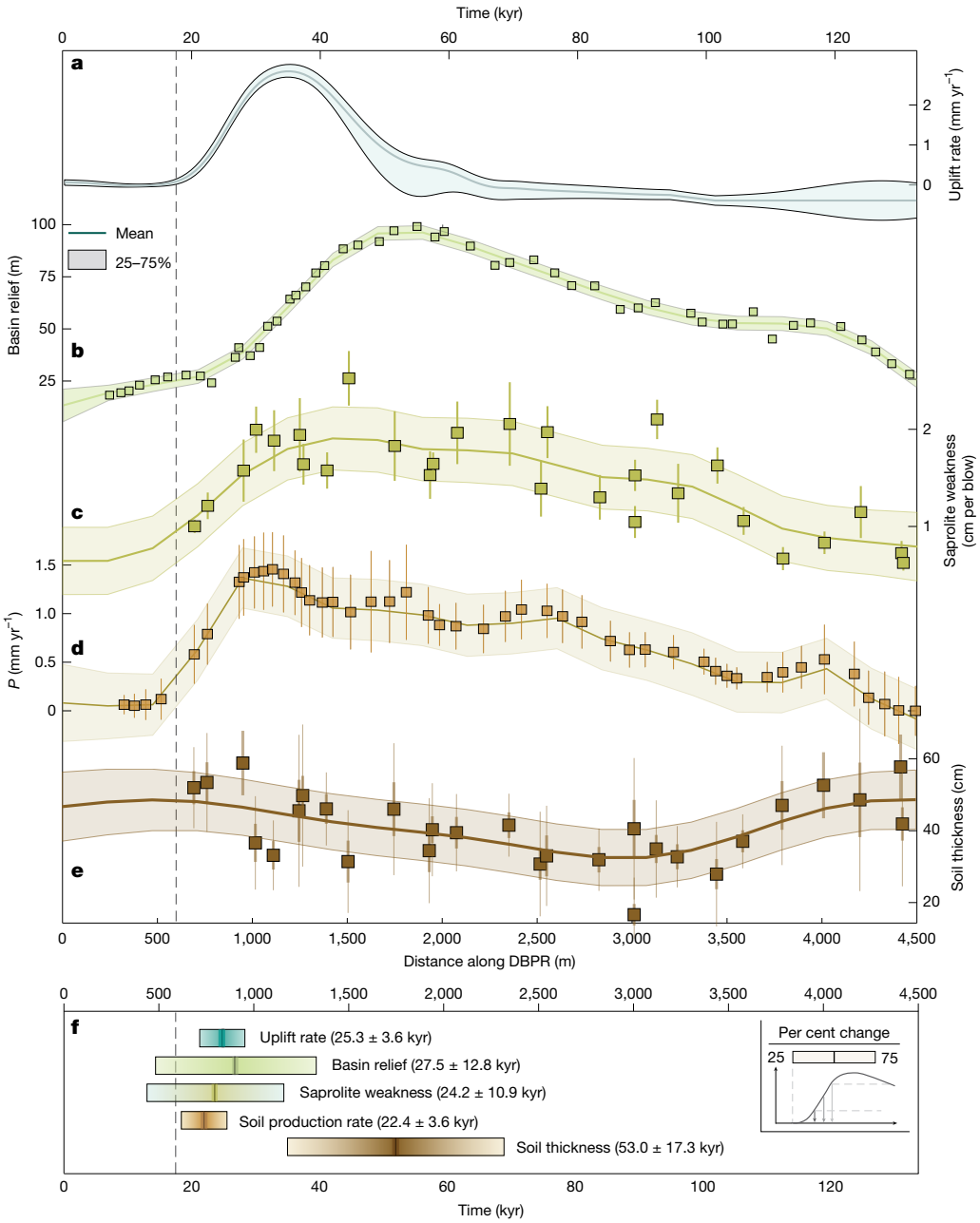

Fig. 4 | Geomorphic evolution at DBPR. a, The transient pulse of uplift (Fig. 2) lasts <40 kyr and reaches a peak uplift rate of 2.8 m kyr^{-1}. The uncertainty envelope represents the 25th–75th percentiles of the MCMC inversion estimates (Fig. 2). We show the uplift rates at the peak of the monoclinal folding geometry shown in Fig. 2f (that is, the maximum uplift observed for each transect perpendicular to the SAF). **b**, The basin relief increases in response to uplift[13]. Each of the squares represents the relief of an individual drainage basin (Fig. 2). **c**, The cone penetrometer observations (Fig. 3) show that the saprolite weakens in response to uplift. The error bars represent the standard error of the saprolite weakness (cm of penetration per strike) at the 6–14 cone penetrometer profiles conducted at each ridgetop transect (Fig. 3b). **d**, The soil production rate increases in tandem with the saprolite becoming weaker. **e**, The soil thickness decreases in response to uplift, but with the longest lag of any of the measured variables. The uncertainty envelopes in **b**–**e** show the ±1σ of the Gaussian process regression models fit to the data points. **f**, Leads and lags in the geomorphic response to uplift. The shaded bars show the time range over which each geomorphic variable undergoes 25%, 50% and 75% of its total change. The uplift rate (**a**), basin relief (**b**), saprolite weakness (**c**) and soil production rate (**d**) all respond with time lags that are within uncertainties of each other, given the constraints of this study. However, the soil thickness change lags the other variables by about 30 kyr, an observation that challenges the notion that soil production rates are controlled by soil thickness (Fig. 1).

the soil thickness of adjacent ridgelines and then apply the space-for-time substitution[13]. For example, the approximately 100 m average catchment spacing at DBPR (Fig. 2b) corresponds to about 3 kyr based on the long-term slip rate on the SAF (Extended Data Fig. 2). Thus, soil thinning by 3 cm from one ridgeline to the next corresponds to $\frac{dH}{dt} = 0.01\,\mathrm{mm\,yr^{-1}}$.

Quantifying surface elevation change from lidar

Comparison of the elevations of adjacent ridgelines across the 50 parallel catchments at DBPR enables calculation of the surface elevation change, $\frac{dz}{dt}$ (Methods). As with the uplift rates and soil thickness changes, we use a space-for-time substitution to convert lateral displacement to time.

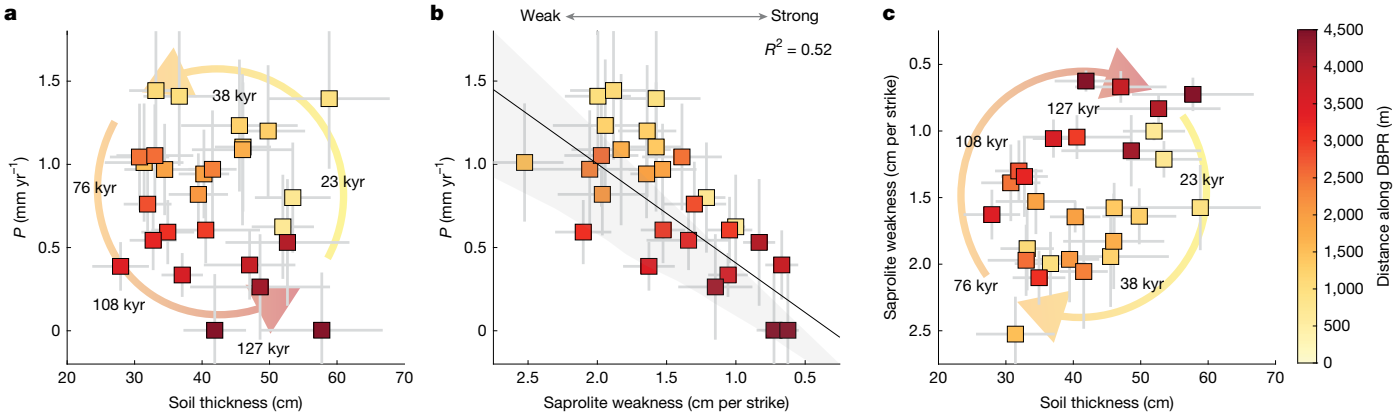

Fig. 5 | Observations of the transient changes to soil production, soil thickness and rock strength. Compare with Fig. 1. **a**, We observe an anticlockwise hysteresis of soil thickness compared with soil production (*P*), indicating that the soil production rate increases before the soil thins (Fig. 4). **b**, Our measurements of rock strength at the soil–saprolite boundary (Fig. 3) show that weaker saprolite yields higher soil production rates[16]. The direct observation from the cone penetrometer surveys is the saprolite weakness (*W*), that is, the penetration distance per strike. *W* varies from 0.5 to 2.5 cm per strike. For consistency with Fig. 1, we plot saprolite weakness on a descending numeric scale so that weak rocks plot on the left and strong rocks plot on the right. In Supplementary Fig. 20, we provide an empirical scaling based on ref. 16 to convert our cone penetrometer measurements (cm per strike) to units of kPa. **c**, We observe a clockwise hysteresis of soil thickness compared with saprolite strength, indicating that saprolite strength is a leading variable and soil thickness is a lagging one.

The result of the (1) uplift inversion, (2) soil thickness measurements and (3) quantification of surface elevation change is a spatially explicit estimate for the rate of soil production, *P*, based on mass conservation (equation (2)).

Measuring rock strength

We use a hand-driven dynamic cone penetrometer to measure saprolite strength[16] at the position of the soil–saprolite boundary (Fig. 3). The penetrometer consists of a fixed weight that is repeatedly lifted 0.91 m up a shaft and then released to hammer the rod into the underlying material. The saprolite weakness is measured in units of cm of penetration per strike, and this quantity is well correlated with the shear strength measured in kPa (ref. 16). We surveyed 28 transects at DBPR with the cone penetrometer. At each transect, we sampled between 6 and 14 sites spanning the southeast, central and northwest sides of the hilltop profiles (Fig. 3b), for a total of 212 cone penetrometer stations.

Leads and lags in the geomorphic response to uplift

In the span of ≤40 kyr, the sedimentary rocks of the Paso Robles Formation undergo about 100 m of uplift (Fig. 4a). This pulse of uplift triggers a cascade of geomorphic changes[13,15], including an increase in basin relief (Fig. 4b), a decrease in saprolite strength (Fig. 4c), an increase in the soil production rate (Fig. 4d) and a decrease in soil thickness (Fig. 4e). After this transient tectonic perturbation, the geomorphic variables relax back to their pre-uplift values over timescales ranging from about 30 to 100 kyr (Fig. 4).

Factors that control the soil production rate

Note in Fig. 4 that the soil thins after the saprolite weakens and the soil production rates increase. In other words, soil thickness cannot be the principal variable driving changes to the rock strength or soil production rate, because the soil thickness change at DBPR occurs too late (Fig. 4).

In Fig. 5, we use the observations from DBPR to test the competing models introduced in Fig. 1. The diagnostic anticlockwise and clockwise hysteresis loops in Fig. 5a and Fig. 5c, respectively, provide the first direct evidence that soil production is regulated not from a top-down, soil-depth control, but rather from the bottom-up (Fig. 1).

Our observations support the following sequence of events at DBPR. First, a pulse of tectonic uplift increases topographic relief, because channel incision keeps pace with uplift[13], whereas erosion at the hilltop lags behind for the 10–30 kyr timescale that it takes for the channel incision to be communicated up the length of the hillslope[13,15]. The increase in topographic relief (Fig. 4b) causes a concomitant reduction in rock strength (Fig. 4c), consistent with model predictions of topographic stresses[7,27] (Extended Data Fig. 10). Finally, the reduction in saprolite strength accelerates the pace of soil production (Fig. 4d), allowing *P* to increase.

More broadly, our data support the hypothesis that soil production is regulated by the strength of the rock at the soil–saprolite boundary[16] (Fig. 5b). This concept of saprolite strength regulating soil production provides a unifying framework that can reconcile the bottom-up and top-down hypotheses. Topographic stresses[7,27] and deep rock weathering[8] are bottom-up mechanisms that modulate rock strength in response to topography rather than soil thickness, consistent with our observations from DBPR. In this model, the accumulation of fractures weakens rock and facilitates weathering such that intact saprolite breaks down to the point of becoming part of the mobile soil layer[30]. Meanwhile, top-down bio-physical disturbance[5,26,30,31] and chemical weathering[4,12,20,21,25] could weaken the saprolite at a rate that depends on the thickness of the soil mantle, providing a top-down control that can co-exist with our bottom-up observations (Extended Data Fig. 10). Although this top-down (soil-thickness-dependent) process cannot be the predominant mechanism for saprolite weakening at DBPR (Figs. 4-5), it could be significant at sites with greater intensities of surface environmental stresses that cause rock fracture and breakdown[30,31] (Extended Data Fig. 10).

Finally, it is important to note that a bottom-up mechanism can support stabilizing feedbacks that allow uplift, erosion and soil production in remain in close balance[1,10,19], even in the absence of a soil-thickness-dependent (top-down) control on soil production (Fig. 1). Through two-dimensional (2D) numerical modelling (Methods), we show that rock strength regulated by topographic stresses[7,27] provides a plausible mechanism that allows *U*, *P* and *E* to keep pace with one another. Specifically, at DBPR, both the valleys and the hilltops experience stresses that can weaken rock through

fracture[27] (Extended Data Fig. 10). Moreover, these stresses scale quasi-linearly with the amplitude of the topography[27]. Put together, these two observations give rise to a stabilizing feedback: the pulse of uplift at DBPR (Fig. 2) leads to an increase in topographic relief (Fig. 4) because channel incision keeps pace with uplift[13], whereas it takes tens of thousands of years for the uplift to be communicated to the hilltops[13,15]. The increase in topographic relief elevates topographic stresses[7,27], weakening the rock and increasing soil production. At the tail end of DBPR, the weakened rock supports high rates of hillslope soil production, but there is no longer a change in base level because the pulse of uplift has ceased. Thus, the hilltop decays relative to the channel, and topographic relief declines. The attenuation in topographic relief reduces the stress weakening the underlying rock, and therefore reduces the rate of soil production.

Implications for landscape evolution

Differentiating between top-down and bottom-up controls on soil production is important both for understanding the feedbacks between landscapes and climate on geological (millennial to million-year) timescales[32,33] and for predicting the sustainability of soil resources on human timescales[19]. For example, as humans accelerate the pace of soil erosion[19,34], a key uncertainty is the degree to which soil production will rise to compensate[19]. The canonical top-down interpretation of the empirical soil production function[2] is that there exists a mechanistic feedback by which thinning soils induces a compensating increase in the rate of soil production[1,2] (Fig. 1b). At DBPR, we find that soil production rises only when tectonic uplift and channel incision lead to an increase in local topographic stresses[7,27], an interpretation that pins the pace of E and P most strongly to the regional tectonic uplift rates[32] (with a role for climate to the extent that climate modulates channel incision[33,35]) rather than the surficial processes that lead to thinning or thickening of the soil mantle.

Soil production is an important process that regulates how landscapes communicate signals from tectonics, climate change and land use. Our observations show that the controls on soil production are more than skin deep; we must look beyond the thickness of the soil layer to explain what regulates the pace of this important bottleneck step in landscape evolution.

Online content

Any methods, additional references, Nature Portfolio reporting summaries, source data, extended data, supplementary information, acknowledgements, peer review information; details of author contributions and competing interests; and statements of data and code availability are available at https://doi.org/10.1038/s41586-025-09751-z.

1. Gilbert, G. K. *Report on the Geology of the Henry Mountains* (US Government Printing Office, 1877).
2. Heimsath, A. M., Dietrich, W. E., Nishiizumi, K. & Finkel, R. C. The soil production function and landscape equilibrium. *Nature* **388**, 358–361 (1997).
3. Larsen, I. J. et al. Rapid soil production and weathering in the Southern Alps, New Zealand. *Science* **343**, 637–640 (2014).
4. West, A. J. Thickness of the chemical weathering zone and implications for erosional and climatic drivers of weathering and for carbon-cycle feedbacks. *Geology* **40**, 811–814 (2012).
5. Roering, J. J., Marshall, J., Booth, A. M., Mort, M. & Jin, Q. Evidence for biotic controls on topography and soil production. *Earth Planet. Sci. Lett.* **298**, 183–190 (2010).
6. Gabet, E. J., Reichman, O. & Seabloom, E. W. The effects of bioturbation on soil processes and sediment transport. *Annu. Rev. Earth Planet. Sci.* **31**, 249–273 (2003).
7. St Clair, J. et al. Geophysical imaging reveals topographic stress control of bedrock weathering. *Science* **350**, 534–538 (2015).
8. Rempe, D. M. & Dietrich, W. E. A bottom-up control on fresh-bedrock topography under landscapes. *Proc. Natl Acad. Sci. USA* **111**, 6576–6581 (2014).
9. Kirkby, M. Hillslope process-response models based on the continuity equation. *Inst. Br. Geogr. Spec. Publ.* **3**, 15–30 (1971).
10. Dietrich, W. E., Reiss, R., Hsu, M.-L. & Montgomery, D. R. A process-based model for colluvial soil depth and shallow landsliding using digital elevation data. *Hydrol. Process.* **9**, 383–400 (1995).
11. Perron, J. T., Kirchner, J. W. & Dietrich, W. E. Formation of evenly spaced ridges and valleys. *Nature* **460**, 502–505 (2009).
12. Ferrier, K. & Perron, J. T. The importance of hillslope scale in responses of chemical erosion rate to changes in tectonics and climate. *J. Geophys. Res. Earth Surf.* **125**, e2020JF005562 (2020).
13. Hilley, G. E. & Arrowsmith, J. R. Geomorphic response to uplift along the Dragon's Back pressure ridge, Carrizo Plain, California. *Geology* **36**, 367–370 (2008).
14. Arrowsmith, J. R. *Coupled Tectonic Deformation and Geomorphic Degradation Along the San Andreas Fault System*. PhD thesis, Stanford Univ. (1995).
15. Hurst, M. D., Mudd, S. M., Attal, M. & Hilley, G. Hillslopes record the growth and decay of landscapes. *Science* **341**, 868–871 (2013).
16. Heimsath, A. M. & Whipple, K. X. Strength matters: resisting erosion across upland landscapes. *Earth Surf. Process. Landf.* **44**, 1748–1754 (2019).
17. Heimsath, A. M., DiBiase, R. A. & Whipple, K. X. Soil production limits and the transition to bedrock-dominated landscapes. *Nat. Geosci.* **5**, 210–214 (2012).
18. Berner, R. A., Lasaga, A. C. & Garrels, R. M. Carbonate-silicate geochemical cycle and its effect on atmospheric carbon dioxide over the past 100 million years. *Am. J. Sci.* 641–683 (1983).
19. Montgomery, D. R. Soil erosion and agricultural sustainability. *Proc. Natl Acad. Sci. USA* **104**, 13268–13272 (2007).
20. Dixon, J. L., Heimsath, A. M. & Amundson, R. The critical role of climate and saprolite weathering in landscape evolution. *Earth Surf. Process. Landf.* **34**, 1507–1521 (2009).
21. Dixon, J. L. & von Blanckenburg, F. Soils as pacemakers and limiters of global silicate weathering. *C. R. Geosci.* **344**, 597–609 (2012).
22. Portenga, E. W. & Bierman, P. R. Understanding Earth's eroding surface with ^{10}Be. *GSA Today* **21**, 4–10 (2011).
23. Culling, W. E. H. Soil creep and the development of hillside slopes. *J. Geol.* **71**, 127–161 (1963).
24. Carson, M. A. & Kirkby, M. J. *Hillslope Form and Process* (Cambridge Univ. Press, 1972).
25. Burke, B. C., Heimsath, A. M. & White, A. F. Coupling chemical weathering with soil production across soil-mantled landscapes. *Earth Surf. Process. Landf.* **32**, 853–873 (2007).
26. Gabet, E. J. & Mudd, S. M. Bedrock erosion by root fracture and tree throw: a coupled biogeomorphic model to explore the humped soil production function and the persistence of hillslope soils. *J. Geophys. Res. Earth Surf.* **115**, F04005 (2010).
27. Miller, D. J. & Dunne, T. Topographic perturbations of regional stresses and consequent bedrock fracturing. *J. Geophys. Res. Solid Earth* **101**, 25523–25536 (1996).
28. Sieh, K. E. & Jahns, R. H. Holocene activity of the San Andreas fault at Wallace Creek, California. *Geol. Soc. Am. Bull.* **95**, 883–896 (1984).
29. Harrison, E. J., Willenbring, J. & Brocard, G. Global rates of soil production independent of soil depth. Preprint at *EarthArXiv* https://eartharxiv.org/repository/view/1946/ (2021).
30. Anderson, S. P. Breaking it down: mechanical processes in the weathering engine. *Elements* **15**, 247–252 (2019).
31. Eppes, M.-C. & Keanini, R. Mechanical weathering and rock erosion by climate-dependent subcritical cracking. *Rev. Geophys.* **55**, 470–508 (2017).
32. Willenbring, J. K. & Jerolmack, D. J. The null hypothesis: globally steady rates of erosion, weathering fluxes and shelf sediment accumulation during Late Cenozoic mountain uplift and glaciation. *Terra Nova* **28**, 11–18 (2016).
33. Perron, J. T. Climate and the pace of erosional landscape evolution. *Ann. Rev. Earth Planet. Sci.* **45**, 561–591 (2017).
34. Wilkinson, B. H. & McElroy, B. J. The impact of humans on continental erosion and sedimentation. *Geol. Soc. Am. Bull.* **119**, 140–156 (2007).
35. Ferrier, K. L., Huppert, K. L. & Perron, J. T. Climatic control of bedrock river incision. *Nature* **496**, 206–209 (2013).

Methods

Quantifying soil production

We use mass conservation to link the bedrock uplift rate, U (L T^{-1}), to the rate of soil production, P (L T^{-1}), the rate of soil thickness change, $\frac{dH}{dt}$ (L T^{-1}) and the rate of surface elevation change, $\frac{dz}{dt}$ (L T^{-1}) (refs. 9,10,23,24). Consider the diagram in Extended Data Fig. 1c. Let z represent the surface elevation, e represent the elevation of the soil–saprolite boundary and H represent the (vertical) soil thickness. The temporal derivatives of these three quantities are related as[10]

$$\frac{dz}{dt} = \frac{de}{dt} + \frac{dH}{dt}. \quad (3)$$

The $\frac{de}{dt}$ term encapsulates the competing effects of rock uplift[36], U, which acts to raise the elevation of the soil–saprolite boundary (e), and soil production, P, which acts to lower e (Extended Data Fig. 1c):

$$\frac{de}{dt} = \frac{\rho_r}{\rho_s}(U - P) \quad (4)$$

where the coefficients ρ_r and ρ_s represent the bulk densities (M L^{-3}) of rock and soil, respectively. Note that we define both P and H in the vertical direction. The slope-normal soil production rate and soil thickness (P_n and h, respectively) can be linked to P and H through the cosine of the hillslope angle, θ (refs. 37,38)

$$P_n = P\cos\theta \quad (5)$$

$$h = H\cos\theta \quad (6)$$

Combining equations (3) and (4), we obtain

$$\frac{dz}{dt} = \frac{\rho_r}{\rho_s}(U - P) + \frac{dH}{dt}. \quad (7)$$

Rearranging for soil production, P, we get

$$P = U - \frac{\rho_s}{\rho_r}\left(\frac{dz}{dt} - \frac{dH}{dt}\right) \quad (8)$$

which is equation (2). Note that, in the equations above, the units of length (L) for the terms $\frac{dH}{dt}$, $\frac{dz}{dt}$ and $\frac{de}{dt}$ refer to bulk densities characteristic of the soil (ρ_s), whereas the units of length for the terms U and P refer to bulk densities characteristic of the rock (ρ_r).

Based on equation (8), the three variables we must independently measure to constrain the soil production rate are $\frac{dH}{dt}$, $\frac{dz}{dt}$ and U. We assume a bulk density ratio of $\frac{\rho_s}{\rho_r} = 0.72 \pm 0.20$, based on compilations of observations from similar bedrock lithologies and from similar upland soils[39–42]. In the following sections, we explain how we constrain each variable in equation (8). Briefly, we use cone penetrometer and GPR observations to constrain soil thickness, lidar data to measure surface elevation, and the elevations of stratigraphic contacts in the Paso Robles Formation to measure the rock uplift. Finally, we take advantage of the unique setting at DBPR, where lateral displacement along the fault corresponds quantitatively to time[13,14,28] (Extended Data Fig. 2) to calculate the timescale for the denominator of the $\frac{dH}{dt}$, $\frac{dz}{dt}$ and U terms.

Evaluating slip rates on the SAF

In our space-for-time substitution, we assume that lateral strike–slip motion along the SAF has remained roughly constant over the past 130 kyr (Fig. 2). Here, we attempt to explore the validity of that assumption using available data. We compile datasets quantifying slip rates on the SAF on decadal to millennial to million-year timescales. On decadal timescales, the fault motion can be measured using GNSS and interferometric synthetic aperture radar (inSAR)[43,44]. On centennial to millennial timescales, fault motion can be quantified through measurements of offset channels[28,45–48] (where the river deposits typically are dated with ^{14}C). On million-year timescales, the fault motion can be quantified from offset volcanic rocks and other piercing points with radiometric age constraints[49–54]. Owing to its abundance of fault-crossing channels[48], the Carrizo Plain has been one of the best-studied sites along the SAF for quantifying historical fault motion[28]. A compilation of the observations of slip rates from the Carrizo Plain and across central California—representing measurement intervals spanning the last decade to the Miocene—suggests that a uniform (spatially and temporally constant) slip rate of 33.0 ± 3.8 mm yr^{-1} represents a reasonable assumption for our modelling of DBPR evolution over the past 130 kyr (Extended Data Fig. 2).

Measuring surface elevation change

We use lidar data from the B4 Lidar Project[55] (see 'Data availability' section) to map surface elevation change. We used the classified point cloud data (sampling density = 2.98 samples m^{-2}) to make a bare Earth digital elevation model (DEM) with a spatial resolution of 0.5 m. As we are interested in quantifying the hilltop soil production, we extracted the elevations of each parallel ridgeline along DBPR (see below for details of the topographic analysis). To compute the rate of elevation change, dz/dt, we differenced the elevation from each ridge to the subsequent ridge (Δz), then measured the lateral distance between the adjacent ridges (Δx). We converted space to time using the long-term slip rates along the SAF[28,45,46] ($\Delta x/\Delta t \approx 33$ mm yr^{-1}). Note that the ridge-to-ridge surface elevation change is not our estimate of the erosion rate. Rather, the erosion rate is the difference between the tectonic uplift (U) and the observed rate of surface elevation change (dz/dt) (Extended Data Fig. 5).

Constraining uplift history

Geological background. The DBPR consists of interbedded siltstones, sandstones and conglomerates of the Paso Robles Formation, a Pliocene–Pleistocene alluvial fan complex sourced from the nearby Temblor Range[14,28] (Extended Data Fig. 1). The Paso Robles Formation can be differentiated into three mapping units: the pink, tan and grey members[13,14,56] (Fig. 2), which have approximate thicknesses of >350 m, 60 m and 20 m, respectively[14]. In the southeast region of DBPR, the topmost unit (grey member) is exposed at the surface. To the northwest, the uplift and subsequent denudation caused by the 'structural knuckle' in the SAF[14], have progressively exposed the underlying tan and pink members (Fig. 2b). Thus, surface mapping of the stratigraphic boundaries can be used to constrain the total amount of rock uplift[36] that has occurred along DBPR[13] (Extended Data Figs. 3 and 4).

Uplift model. We used field observations, lidar data and high-resolution National Agriculture Imagery Program imagery to refine previous maps of the DBPR region[13,14,56] (see 'Data Availability' section) and better constrain the precise (x, y, z) positions of the contacts between the pink, tan, and grey members of the Paso Robles Formation (Fig. 2b). We then used an MCMC framework to invert these geological constraints into probabilistic estimates of the spatial pattern of uplift (Extended Data Figs. 3 and 4). In particular, we use the MCMC inversion procedure to evaluate the sensitivity of inferred uplift to the three main sources of uncertainty in our uplift model: (1) the stratigraphic thickness of the middle (tan) member of the Paso Robles Formation; (2) the starting (pre-uplift) elevation of the tan–grey contact; and (3) the location of the inflection in the approximately monoclinal folding geometry constrained by structural (strike and dip) measurements[14] (Extended Data Fig. 3). We perform a systematic exploration of the parameter space to investigate what combinations of these three geometrical parameters can best explain the geological observations (the strike-and-dip

measurements[14] and the (x, y, z) positions of the mapped stratigraphic contacts) (Extended Data Fig. 4). All three parameters are assumed to be uniform (constant) across space.

Our inversions show that there are trade-offs between the three unknown parameters (Extended Data Fig. 4). For example, the scenario in which the tan member is thicker and the original (pre-uplift) elevation of the pink–tan boundary is lower can explain the geological data approximately equally well as the scenario in which the tan member is thinner and the pre-uplift elevation of the pink–tan boundary is higher (Extended Data Fig. 4). The MCMC framework allows us to propagate these correlated trade-offs and generate a probabilistic uplift map with associated uncertainties (Fig. 2 and Extended Data Fig. 8).

Differentiating between subsidence and non-steady uplift. In the uplift model shown in Fig. 2, the total rock uplift decreases in the northwest region of the study area (that is, the region that has had the longest duration since passing through the structural knuckle[13,14]). This observation also appears in the uplift reconstructions in ref. 13, and it derives from the fact that the elevation of the stratigraphic contacts (between the pink, tan and grey members of the Paso Robles Formation) decrease across the final 2 km of DBPR (Fig. 2). There are two scenarios that could give rise to this observation of a distal decrease in elevation: (1) non-steadiness in uplift and (2) subsidence. The first scenario postulates that, approximately 60–120 kyr ago when the drainage basins in the northwest corner of DBPR were in the peak uplift zone (Fig. 2h), the geometry of the structural knuckle[14] was such that rocks were uplifted less than the approximately 2.5 mm of vertical uplift for every 33 mm if horizontal translation[28]—the values observed for the Holocene and latest Pleistocene[13,28] (Extended Data Fig. 2). According to this scenario, the bedrock at the northwest end of DBPR only experienced around 70 m of maximum uplift, in contrast to the approximately 90 m of uplift experienced by the bedrock currently located in the central zone of DBPR (Fig. 2). The second possibility is that rates of vertical uplift and lateral translation at the structural knuckle have remained constant over the last 140 kyr, but that the geometry of the fault offset is such that it leads to subsequent subsidence in the lee of the structural knuckle. In this scenario, the rocks at the northwest end of DBPR experienced the same 90 m maximum uplift observed today, but have since subsided by about 20 m. These two scenarios have different implications for the time histories of the hillslopes and drainage basins along DBPR[13,15].

To differentiate between the non-steady uplift scenario and the subsequent subsidence scenario, we consider the spatial pattern of elevation change distal to the SAF. The sediments eroded from the hilltops, hillslopes and bedrock channels within each of the DBPR drainages are deposited at the valley floor (Carrizo Plain). Proximal to each drainage basin outlet, this sedimentary flux can be detected as an increase in the elevation of the valley floor (Extended Data Fig. 5a). However, beyond a distance of about 400 m from the SAF, the elevation change in the valley floor between the pre-uplift and the maximum uplift zones of DBPR is ≤3 m. Thus, we propose that the elevation at 410 m distance from SAF is largely unaffected by the sedimentary flux from the DBPR basins and instead tracks regional subsidence. Elevation profiles at 410 m indicate approximately 18 m of subsidence in the northwest region of DBPR (Extended Data Fig. 5), consistent with the estimates for the reduction in cumulative rock uplift produced by the uplift model. Thus, we favour the scenario of subsequent subsidence rather than non-steadiness in uplift to explain the 20 m reduction in cumulative uplift observed across the last 1–2 km of DBPR (Fig. 2f).

Field observations of saprolite strength and soil thickness

We constrained saprolite strength and soil thickness across DBPR through cone penetrometer measurements, soil pits and GPR surveys. Extended Data Fig. 6 shows the locations of our 212 cone penetrometer stations and 22 hand-dug soil pits at DBPR. Supplementary Tables 2 and 5 provide the soil pit and cone penetrometer observations, respectively, in tabular form.

Cone penetrometer surveys. We quantified saprolite strength using a hand-driven dynamic cone penetrometer[16]. The penetrometer consists of a fixed weight that is repeatedly lifted 91 cm up a shaft and then released to hammer the rod into the underlying material. Thus, the weakness of the subsurface material is measured in terms of the cm of penetration per strike. Extended Data Fig. 7 shows examples of the cone penetrometer observations at 5 of the 28 penetrometer transects. Each cone penetrometer profile is visualized in a manner akin to a stratigraphic column, where the y-axis represents depth below the surface, and the x-axis represents the regolith weakness (reported in units of cm of penetration per strike). The transition from weak to strong regolith is interpreted as the soil–saprolite boundary, an interpretation that is supported by textural and sedimentological observations from co-located soil pits (Fig. 3e). We identify the transition from weak to strong regolith using a simple quantitative criterion (identifying the horizon at which the regolith weakness falls below $1/e \approx 37\%$ of its maximum value). We then extract the regolith weakness value at and below the position of the soil–saprolite boundary. We refer to this quantity as the 'saprolite weakness' (Supplementary Table 5).

Previous studies have shown that the penetrometer weakness is well correlated with the regolith shear strength[16,57] (for example, measured in units of kPa). We can use the empirical relationship between penetrometer weakness and shear strength quantified in ref. 16 to convert our saprolite weakness measurements in Fig. 5 to units of kPa. The results of this conversion are shown in Supplementary Figs. 19 and 20. However, the conversion from units of cm per strike to kPa was not independently calibrated in this study and should be viewed only as an order-of-magnitude-type approximation. Our conclusions are insensitive to the choice of expressing the saprolite weakness in terms of cm per strike compared with kPa, and the cone penetrometer data are shown in their original units (cm per strike) in the main text.

We surveyed 28 transects with the cone penetrometer. At each transect, we sampled between 6 and 14 sites spanning the southeast, central, and northwest sides of the ridgetop profiles, for a total of 212 cone penetrometer stations (Supplementary Table 5). At 21 of the 28 cone penetrometer transect locations, we collected simultaneous GPR profiles (Fig. 3a–c).

Soil pit observations. We dug 22 soil pits across the length of the DBPR and made observations of grain size, sorting, lithification and sedimentary fabric (for example, bedding and bioturbation) in each pit. We searched for the horizon at which the poorly lithified Paso Robles Formation sediments lost their primary bedding and adopted the churned, poorly sorted fabric of the overlying soil. We defined this horizon, which is based on textural properties, as the soil–saprolite boundary. These soil thickness observations served as the ground truth to validate and interpret the cone penetrometer data (Fig. 3e). See Extended Data Fig. 6c for stratigraphic columns representing each soil pit. Example photographs of the soil pits are shown in Extended Data Fig. 9.

Measuring soil thickness with GPR

We build on the success of previous studies[5,58–60] and develop a workflow for mapping the soil–saprolite boundary using GPR. Our methodology includes classical GPR processing steps, in addition to a neural network approach for identifying the soil–saprolite boundary from the shape of the GPR waveform. See the Supplementary Information for a detailed description of our GPR data acquisition and analysis. We use co-located GPR and cone penetrometer observations to calibrate and validate the GPR-based soil thickness estimates (Extended Data Fig. 6d). Extended Data Fig. 7 shows an example set of cone penetrometer observations and associated GPR waveforms. A cross-plot comparing the soil thickness estimates from the cone penetrometer compared with the GPR is

shown in Extended Data Fig. 6f. The R^2 of this relationship is 0.86, the mean absolute error is 0.04 m, and the bias is 0.01 m.

Topographic analysis

Figure 4 shows geomorphic parameters—including the basin relief, saprolite strength, soil production rate and soil thickness—extracted for each of the parallel ridges and drainage basins that comprise the DBPR. To quantify these attributes for each ridgeline and/or drainage basin, we used lidar digital elevation data[55] to segment the channel networks and associated drainage basins. We used TopoToolbox[61] to extract the channel networks, using the multiple flow direction methodology for partitioning flow to all downward neighbours according to slope. We used Geonet[62] to identify the channel heads according to the geometric method in ref. 63. We identified the ridges in the lidar DEM as the intersections between adjacent drainage basins[64]. We define 'basin relief' (Fig. 4) as the difference between the maximum and minimum elevation in each drainage basin (Fig. 2a).

Error propagation

Note that, based on equation (2), the uncertainties associated with the uplift rate reconstruction (U), the bulk density ratio (ρ_s/ρ_r), the rate of elevation change ($\frac{dz}{dt}$) and the rate of soil thickness change ($\frac{dH}{dt}$) all combine to set the uncertainty of the estimated soil production rate, P. In section 3 of the Supplementary Information, we perform an error propagation analysis to quantify the uncertainty on P. Extended Data Fig. 8a,b shows the uncertainties associated with the cumulative uplift and uplift rate reconstructions, and Extended Data Fig. 8c shows the uncertainty estimated for P, which is on the order of 30%. See the Supplementary Information for more details.

Testing for lithological controls

In Fig. 2, the stratigraphic member of the Paso Robles Formation that is present at the surface (beneath the soil layer) changes systematically from the grey member to the tan member to the pink member[13,14,56]. This progression prompts us to investigate whether the spatial changes in saprolite strength or soil thickness (Fig. 4) are caused by changes in the underlying bedrock lithology rather than the transient geomorphic response to uplift.

We find that the distance along DBPR is the primary control on saprolite strength and soil thickness, rather than the stratigraphic member in the Paso Robles Formation. For example, Extended Data Fig. 8d compiles the soil thickness measurements—from both the cone penetrometer and GPR surveys—and colour-codes the observations according to the exposed stratigraphic member of the Paso Robles Formation. Closely spaced observations from two different stratigraphic members show little difference in soil thickness. In other words, we find no evidence that the soils overlying the closely spaced grey, tan or pink members of the Paso Robles Formation are systematically thinner or thicker (Extended Data Fig. 8d).

Testing for consistency across different soil thickness datasets

Soil thickness datasets. In this study, we collected three sets of soil thickness observations. The first dataset is the (spatially limited) set of hand-dug soil pits (Extended Data Figs. 6b,c and 9). This dataset is useful for documenting the textural character and composition of the soils along DBPR and for validating the cone-penetrometer-based measurements of soil thickness (Fig. 3e). However, the labour-intensive and time-consuming nature of this measurement, in addition to the qualitative (observer-dependent) classification of the soil–saprolite boundary (Supplementary Table 2), limits the utility of the soil pits for mapping large-scale changes in soil thickness.

The second soil thickness dataset is from our network of cone penetrometer stations (n = 212), located at 28 different ridgetop transects (Extended Data Fig. 6). Each transect consists of 6–14 cone penetrometer profiles, allowing us to average some of the local (metre-scale) spatial heterogeneity and better document long-term trends in soil thickness. Two main advantages of the cone penetrometer measurements are that they (1) represent the direct physical probing into the subsurface and (2) provide a set of quantitative observations (strike counts and penetration depths) that allow for the objective classification of the soil–saprolite boundary (Extended Data Fig. 7), rather than the qualitative identification from the hand-dug soil pits. Still, the cone penetrometer transects represent a spatially limited set of soil thickness observations.

The third soil thickness dataset is from the GPR. The principal advantage of GPR is its ability to map large distances and acquire large numbers of observations. For example, the 19 km of GPR profiles acquired in this study represent 744,928 individual pings, 628,298 of which could be converted to estimates of soil thickness along the DBPR using our neural network (Extended Data Fig. 8d). The principal disadvantage of the GPR dataset is that it is a form of remote sensing; the soil–saprolite boundary is not directly probed or observed, but rather inferred based on the shape and structure of the GPR waveform. Note that the soil thickness estimates from GPR are not independent of the soil thickness estimates from the cone penetrometer, since we use the cone penetrometer observations as ground truth to train the machine learning model that locates the soil–saprolite boundary from the shape of the GPR waveforms (Supplementary Information section 1).

Is our key observation robust across different soil thickness datasets? As shown in Fig. 1, the principal observation we use in this study to test the validity of the top-down and bottom-up controls on soil production is the directionality (clockwise or anticlockwise) of the h–P (soil thickness and soil production rate) and h–S (soil thickness and saprolite strength) hystereses (Figs. 1 and 5). Here, we show that our findings are robust (insensitive) to which soil thickness dataset we use.

In Fig. 5, we use soil thickness estimates from the cone penetrometer transects. As the hand-dug soil pits were only collected at n = 7 different distances along DBPR (they were collected as sets of three closely spaced pits, each separated approximately 10 m apart; see Extended Data Fig. 6), we do not have enough data to produce crossplots such as Fig. 5 using soil thickness data from the hand-dug soil pits alone. However, the GPR observations provide a spatially extensive dataset of soil thickness that can be used to produce an analogous version of Fig. 5. The results are shown in Extended Data Fig. 8. Note that Fig. 5b and Extended Data Fig. 8f are identical, because these panels do not involve soil thickness measurements. However, the first and last panels are different because the soil thickness estimates come from the cone penetrometer observations (Fig. 5) and the GPR observations (Extended Data Fig. 8). Importantly, note that both figures show an anticlockwise hysteresis of soil thickness compared with soil production rate, and a clockwise hysteresis of soil thickness compared with saprolite strength. In other words, our findings supporting a bottom-up mechanism for soil production are robust with respect to the soil thickness dataset used.

Feedbacks coupling uplift and soil production in a bottom-up model

It has long been recognized[1] that there must be a mechanism keeping uplift, erosion and soil production in close balance[1,10,19]. Otherwise, according to equation (1), soils would either disappear or accumulate to be much thicker than the relatively uniform 0.1–2.0-m-thick soil layer observed across most of the surface of Earth[19]. The top-down scenario, by which soil thickness sets the pace of soil production[2] (Fig. 1b,c), provides an effective self-arresting feedback; if erosion outpaces soil production, then soils thin, causing the rate of soil production to increase and come into balance with erosion. Likewise, if erosion is slower than soil production, soil thickness will increase and soil production will slow down (Fig. 1b). It is perhaps less intuitive that a bottom-up scenario would allow for the same type of self-arresting behaviour.

Here, we explore a plausible negative feedback for the bottom-up scenario, which arises from the influence of topographic stresses on rock strength and fracturing[7,27,30,65–67].

Topographic stress and rock strength: background. Consistent with the framework of ref. 30, the mechanism explored here begins with the premise that fracturing rock is a prerequisite for soil production. Fractures in bedrock facilitate soil production and erosion by providing pathways for chemical weathering[8,68], increasing the efficiency of fluvial and glacial erosion[66,67,69–72] and reducing slope stability[65,73–75]. It seems that fracture density—more so than the intrinsic strength of the intact rock[76]—is the main variable explaining variations in hillslope form and soil production[65,75–79]. Thus, in this framework, a negative feedback for soil production in the bottom-up scenario could be a mechanism that explains why landscapes with higher uplift rates would have more bedrock fracturing. Two related mechanisms—tectonic stresses and topographic stresses—allow for this self-arresting behaviour (Extended Data Fig. 10a,b).

Tectonic stresses. As articulated in ref. 67, the simple geometric constraint that dip-slip faults that approach the surface must be bent rather than planar[80,81] implies that rocks in tectonically active convergent settings must undergo substantial strain. In the brittle part of the crust, this strain results in rock fracture[67]. Thus, ref. 67 explains as follows: '… in tectonically active regions … dismembered rock arrives at the Earth's surface already prepared to be transported away.' This hypothesis has been supported by more recent work from locations such as the Southern Alps in New Zealand[65,75] and the San Gabriel Mountains and San Jacinto Mountains in California[78] demonstrating that higher uplift areas have denser and deeper-penetrating bedrock fractures[65,75,78].

Topographic stresses. Topographic stresses allow for a more dynamic interaction between soil production and erosion rates than the tectonic stress mechanism described above. A feedback based on topographic stresses is based on the concept that the landscape itself may influence the location and abundance of fractures forming in the bedrock by changing the ambient stress field[27,66,67,82,83]. Previous studies[83,84] showed that, to first order, the magnitude of topographic stresses scales as $\rho g b$, where ρ is the rock density, g is the gravitational acceleration, and b is the ridge height or valley depth. In other words, topographic stresses scale quasi-linearly with the relief of the topography. Another study[27] applied the analytical solution of refs. 83,84 to show that such topographic stresses are sufficient to fracture bedrock. This study[27] explained, 'By perturbing the state of stress, landforms themselves may become fracture-forming agents, initiating feedbacks between regional stresses and the bedrock properties that govern processes of erosion and landscape evolution.'

Fracturing valleys compared with fracturing hilltops. Most topographic stress modelling has focused on how topography causes amplified stresses in the valleys[27,66,69,70,85]. For example, ref. 27 noted that valley incision amplifies fracturing at the valley floor (as elastic stresses scale with topographic relief[27,84]), which makes bedrock more erodible[69] and should further increase valley incision. However, this scenario of a positive feedback loop between valley incision, increased differential stress, fracturing, and further valley incision implies a runaway on landscape relief unless there is a mechanism by which increased valley incision also triggers increased fracturing on the hillslopes and hilltops. Previous studies[86–88] provide a plausible mechanism by noting that regional compressive stresses (the norm for upland landscapes) induce tension along traction-free surfaces (that is, the land surface) in convex parts of the topography. For example, for a cylindrical surface geometry, the tension normal to the surface (T) is

$$T = k\sigma_P - \rho g \cos\beta \quad (9)$$

where k (m^{-1}) is the curvature (inverse of the radius of curvature), σ_P (MPa) is the compressive stress parallel to the convex surface, ρ (kg m^{-3}) is the density of rock, g (m s^{-2}) is the gravitational acceleration, and β is the surface slope[86]. The formulation can be extended to two dimensions[87]:

$$T = k_1\sigma_{11} + k_2\sigma_{22} - \rho g \cos\beta \quad (10)$$

where k_1 and k_2 (m^{-1}) are the principal curvatures and σ_{11} and σ_{22} (MPa) are the stresses parallel to the principal curvatures[87]. The tension imparted on the convex ridges can produce opening-mode fractures, complementing the shear fractures generated in the valleys (Extended Data Fig. 10).

Numerical modelling and boundary-element simulations. We perform a simple set of 2D topographic stress modelling experiments (using boundary-element simulations[85,89]) to test whether the topography at DBPR is sufficient to fracture rock, not only in the valleys[27] but also at the hilltops[86–88]. Extended Data Fig. 10 shows a 2D cross-section of ridge and valley topography at the same scale as observed at DBPR. We use the boundary-element simulation to compute the stresses in each direction σ_{xx}, σ_{yy} and σ_{xy}, and then reconstruct the principal stresses σ_1 and σ_3. Finally, we quantify the propensity for shear fractures and opening-mode fractures. Following ref. 85, we calculate the minimum cohesion required to prevent shear failure, C_{min} (MPa), as a proxy for the propensity for producing shear fractures. Likewise, in the parts of the terrain susceptible to mode I (opening mode) fractures, we calculate the opening tension, T_{open} (MPa) (Extended Data Fig. 10i,j). Note that rocks are much weaker in response to tensile stresses than to normal stresses (Extended Data Fig. 10k), so $T_{open} < C_{min}$.

Summary: tectonic-topographic stresses and a stabilizing feedback for landscape evolution. We find that, for the topography observed at DBPR and under plausible scenarios of regional tectonic compression, σ_{tect}, both the valleys and the hilltops experience stresses that can fracture rock (Extended Data Fig. 10). Moreover, to first order, these stresses scale with the amplitude of the topography[27,83,84,87,88]. Put together, these two observations give rise to a stabilizing feedback that can explain how soil production keeps pace with erosion (Fig. 5), even in the absence of a soil-thickness-dependent (top-down) control on soil production. The proposed feedback goes as follows: the pulse of uplift at DBPR (Fig. 2) leads to an increase in topographic relief (the ridge-to-valley relief) because channel incision keeps pace with uplift with only a small temporal lag (of the order of a few kyr; ref. 13), whereas it takes approximately 10 times longer for the uplift to be communicated up the hillslopes to the hilltops[90] (temporal lag of the order of about 70 kyr; refs. 13,15). The increase in topographic relief causes the rates of both hillslope sediment transport and soil production to increase. For example, as the lateral basin spacing cannot adjust rapidly (it requires the much slower process of basin capture; Fig. 2a), the increase in topographic relief provokes an increase in hillslope gradient and associated sediment transport[9,10,23,24]. Meanwhile, the topographic stresses[27,83,84] also respond roughly proportionally to the increase in topographic relief, weakening the rock and increasing soil production. On the tail end of DBPR, the weakened rock supports more efficient hillslope soil production, but there is no longer a change in base level at the channel bottom because the pulse of uplift has ceased. Thus, the hilltop decays relative to the channel, and topographic relief attenuates. The attenuation in topographic relief reduces the topographic stresses and, therefore, leads to a reduction in the rate of soil production.

Data availability

All data generated and analysed in this study—including our raw and processed GPR observations, cone penetrometer data, updated

geological map, uplift inversions and the geomorphic parameters shown in Figs. 4 and 5—are available at Zenodo[91] (https://doi.org/10.5281/zenodo.12637755). The lidar dataset is from the National Center for Airborne Laser Mapping and is available on OpenTopography. The geological map of Dibblee (1973, 1999) is available from the US Geological Survey (https://pubs.usgs.gov/of/1999/of99-014/).

Code availability

The MATLAB code developed for this study is available at Zenodo[91] (https://doi.org/10.5281/zenodo.12637755). We used the open-source GPRPy software of Alain Plattner (https://github.com/NSGeophysics/GPRPy) to process the GPR data. We used TopoToolbox (https://topotoolbox.wordpress.com/)[61] to extract the basins and channel networks from the lidar digital elevation data, and Geonet (https://sites.google.com/site/geonethome/)[62] to identify the channel heads (following the geometric method in ref. 63). Finally, we used the boundary element model adapted from ref. 89 to model topographic stresses.

36. England, P. & Molnar, P. Surface uplift, uplift of rocks, and exhumation of rocks. *Geology* **18**, 1173–1177 (1990).
37. Heimsath, A. M., Dietrich, W. E., Nishiizumi, K. & Finkel, R. C. Stochastic processes of soil production and transport: Erosion rates, topographic variation and cosmogenic nuclides in the Oregon Coast Range. *Earth Surf. Process. Landf.* **26**, 531–552 (2001).
38. Roering, J. J. How well can hillslope evolution models explain topography? Simulating soil transport and production with high-resolution topographic data. *Geol. Soc. Am. Bull.* **120**, 1248–1262 (2008).
39. Anderson, S. P., Dietrich, W. E. & Brimhall Jr, G. H. Weathering profiles, mass-balance analysis, and rates of solute loss: Linkages between weathering and erosion in a small, steep catchment. *Geol. Soc. Am. Bull.* **114**, 1143–1158 (2002).
40. Hayes, J. L., Riebe, C. S., Holbrook, W. S., Flinchum, B. A. & Hartsough, P. C. Porosity production in weathered rock: Where volumetric strain dominates over chemical mass loss. *Sci. Adv.* **5**, eaao0834 (2019).
41. Yoo, K., Amundson, R., Heimsath, A. M. & Dietrich, W. E. Process-based model linking pocket gopher (*Thomomys bottae*) activity to sediment transport and soil thickness. *Geology* **33**, 917–920 (2005).
42. Manger, G. E. *Porosity and Bulk Density of Sedimentary Rocks*. Technical Report (US Geological Survey, 1963).
43. Tong, X., Sandwell, D. & Smith-Konter, B. High-resolution interseismic velocity data along the San Andreas Fault from GPS and InSAR. *J. Geophys. Res. Solid Earth* **118**, 369–389 (2013).
44. Savage, J. C. Strain accumulation in western United States. *Ann. Rev. Earth Planet. Sci.* **11**, 11–41 (1983).
45. Noriega, G. R., Arrowsmith, J. R., Grant, L. B. & Young, J. J. Stream channel offset and late Holocene slip rate of the San Andreas fault at the Van Matre ranch site, Carrizo Plain, California. *Bull. Seismol. Soc. Am.* **96**, 33–47 (2006).
46. Liu-Zeng, J., Klinger, Y., Sieh, K., Rubin, C. & Seitz, G. Serial ruptures of the San Andreas fault, Carrizo Plain, California, revealed by three-dimensional excavations. *J. Geophys. Res. Solid Earth* **111**, B02306 (2006).
47. Grant Ludwig, L., Akciz, S. O., Arrowsmith, J. R. & Salisbury, J. B. Reproducibility of San Andreas fault slip rate measurements at Wallace Creek in the Carrizo Plain, CA. *Earth Space Sci.* **6**, 156–165 (2019).
48. Dascher-Cousineau, K., Finnegan, N. J. & Brodsky, E. E. The life span of fault-crossing channels. *Science* **373**, 204–207 (2021).
49. Gooley, J. T., Sharman, G. R. & Graham, S. A. Reconciling along-strike disparity in slip displacement of the San Andreas fault, central California, USA. *Geol. Soc. Am. Bull.* **133**, 1441–1464 (2021).
50. Huffman, O. F. Lateral displacement of upper Miocene rocks and the Neogene history of offset along the San Andreas fault in central California. *Geol. Soc. Am. Bull.* **83**, 2913–2946 (1972).
51. Ryder, R. T. & Thomson, A. *Tectonically Controlled Fan Delta and Submarine Fan Sedimentation of Late Miocene Age, Southern Temblor Range, California*. Professional Paper 1442 (US Geological Survey, 1989).
52. Stanley, R. G., Barron, J. A. & Powell II, C. L. *Evaluation of Hypotheses for Right-Lateral Displacement of Neogene Strata Along the San Andreas Fault Between Parkfield and Maricopa, California*. Report No. 2017-5125 (US Geological Survey, 2017).
53. Stanley, R. G. New estimates of displacement along the San Andreas fault in central California based on paleobathymetry and paleogeography. *Geology* **15**, 171–174 (1987).
54. Graham, S., Stanley, R. G., Bent, J. & Carter, J. Oligocene and Miocene paleogeography of central California and displacement along the San Andreas fault. *Geol. Soc. Am. Bull.* **101**, 711–730 (1989).
55. Bevis, M. & Hudnut, K. *B4 Lidar Project: Airborne Laser Swath Mapping (ALSM) Survey of the San Andreas Fault (SAF) System of Central and Southern California, Including the Banning Segment of the SAF and the San Jacinto Fault System*. Technical. Report, National Center for Airborne Laser Mapping (NCALM), US Geological Survey, the Ohio State University and the Southern California Integrated GPS Project (US Geological Survey, 2005).
56. Dibblee, T. et al. *Regional Geologic Map of San Andreas Fault and Related Faults and Carrizo Plain, Temblor, Caliente, and La Panza Ranges and Vicinity, California*. US Geological Survey Miscellaneous Geological Investigations, Map I-757, Scale 1:125,000 (US Geological Survey, 1973).
57. Bachmann, J., Contreras, K., Hartge, K. & MacDonald, R. Comparison of soil strength data obtained in situ with penetrometer and with vane shear test. *Soil Tillage Res.* **87**, 112–118 (2006).
58. Sucre, E. B., Tuttle, J. W. & Fox, T. R. The use of ground-penetrating radar to accurately estimate soil depth in rocky forest soils. *For. Sci.* **57**, 59–66 (2011).
59. Dal Bo, I. et al. Geophysical imaging of regolith in landscapes along a climate and vegetation gradient in the Chilean coastal cordillera. *Catena* **180**, 146–159 (2019).
60. Schaller, M. et al. Comparison of regolith physical and chemical characteristics with geophysical data along a climate and ecological gradient, Chilean Coastal Cordillera (26–38° S). *Soil* **6**, 629–647 (2020).
61. Schwanghart, W. & Kuhn, N. J. TopoToolbox: a set of MATLAB functions for topographic analysis. *Environ. Model. Softw.* **25**, 770–781 (2010).
62. Sangireddy, H., Stark, C. P., Kladzyk, A. & Passalacqua, P. Geonet: an open source software for the automatic and objective extraction of channel heads, channel network, and channel morphology from high resolution topography data. *Environ. Model. Softw.* **83**, 58–73 (2016).
63. Passalacqua, P., Do Trung, T., Foufoula-Georgiou, E., Sapiro, G. & Dietrich, W. E. A geometric framework for channel network extraction from lidar: nonlinear diffusion and geodesic paths. *J.Geophys. Res. Earth Surf.* **115**, F01002 (2010).
64. Hurst, M. D., Mudd, S. M., Walcott, R., Attal, M. & Yoo, K. Using hilltop curvature to derive the spatial distribution of erosion rates. *J. Geophys. Res. Earth Surf.* **117**, F02017 (2012).
65. Clarke, B. A. & Burbank, D. W. Quantifying bedrock-fracture patterns within the shallow subsurface: implications for rock mass strength, bedrock landslides, and erodibility. *J. Geophys. Res. Earth Surf.* **116**, F04009 (2011).
66. Molnar, P. Interactions among topographically induced elastic stress, static fatigue, and valley incision. *J. Geophys. Res. Earth Surf.* **109**, F02010 (2004).
67. Molnar, P., Anderson, R. S. & Anderson, S. P. Tectonics, fracturing of rock, and erosion. *J. Geophys. Res. Earth Surf.* **112**, F03014 (2007).
68. Anderson, S. P., von Blanckenburg, F. & White, A. F. Physical and chemical controls on the critical zone. *Elements* **3**, 315–319 (2007).
69. Whipple, K. X., Hancock, G. S. & Anderson, R. S. River incision into bedrock: mechanics and relative efficacy of plucking, abrasion, and cavitation. *Geol. Soc. Am. Bull.* **112**, 490–503 (2000).
70. Augustinus, P. C. Glacial valley cross-profile development: the influence of in situ rock stress and rock mass strength, with examples from the Southern Alps, New Zealand. *Geomorphology* **14**, 87–97 (1995).
71. Leith, K., Moore, J. R., Amann, F. & Loew, S. In situ stress control on microcrack generation and macroscopic extensional fracture in exhuming bedrock. *J. Geophys. Res. Solid Earth Surf.* **119**, 594–615 (2014).
72. Leith, K., Moore, J. R., Amann, F. & Loew, S. Subglacial extensional fracture development and implications for Alpine Valley evolution. *J. Geophys. Res. Earth Surf.* **119**, 62–81 (2014).
73. Li, G. K. & Moon, S. Topographic stress control on bedrock landslide size. *Nat. Geosci.* **14**, 307–313 (2021).
74. Muller, J. R. & Martel, S. J. Numerical models of translational landslide rupture surface growth. *Pure Appl. Geophys.* **157**, 1009–1038 (2000).
75. Clarke, B. A. & Burbank, D. W. Bedrock fracturing, threshold hillslopes, and limits to the magnitude of bedrock landslides. *Earth Planet. Sci. Lett.* **297**, 577–586 (2010).
76. Selby, M. J. A rock mass strength classification for geomorphic purposes: with tests from Antarctica and New Zealand. *Z. Geomorphol.* **24**, 31–51 (1980).
77. DiBiase, R. A., Rossi, M. W. & Neely, A. B. Fracture density and grain size controls on the relief structure of bedrock landscapes. *Geology* **46**, 399–402 (2018).
78. Neely, A. B., DiBiase, R. A., Corbett, L. B., Bierman, P. R. & Caffee, M. W. Bedrock fracture density controls on hillslope erodibility in steep, rocky landscapes with patchy soil cover, southern California, USA. *Earth Planet. Sci. Lett.* **522**, 186–197 (2019).
79. Neely, A. B. & DiBiase, R. A. Drainage area, bedrock fracture spacing, and weathering controls on landscape-scale patterns in surface sediment grain size. *J. Geophys. Res. Earth Surf.* **125**, e2020JF005560 (2020).
80. Suppe, J. Geometry and kinematics of fault-bend folding. *Am. J. Sci.* **283**, 684–721 (1983).
81. Suppe, J. *Principles of Structural Geology* (Prentice Hall, 1985).
82. McTigue, D. F. & Mei, C. C. Gravity-induced stresses near topography of small slope. *J. Geophys. Res. Solid Earth* **86**, 9268–9278 (1981).
83. Savage, W. Z. & Swolfs, H. S. Tectonic and gravitational stress in long symmetric ridges and valleys. *J. Geophys. Res. Solid Earth* **91**, 3677–3685 (1986).
84. Savage, W. Z., Swolfs, H. S. & Powers, P. S. Gravitational stresses in long symmetric ridges and valleys. *Int. J. Rock Mech. Min. Sci. Geomech. Abstr.* **22**, 291–302 (1985).
85. Slim, M., Perron, J. T., Martel, S. J. & Singha, K. Topographic stress and rock fracture: A two-dimensional numerical model for arbitrary topography and preliminary comparison with borehole observations. *Earth Surf. Process. Landf.* **40**, 512–529 (2015).
86. Martel, S. J. Effect of topographic curvature on near-surface stresses and application to sheeting joints. *Geophys. Res. Lett.* **33**, L01308 (2006).
87. Martel, S. J. Mechanics of curved surfaces, with application to surface-parallel cracks. *Geophys. Res. Lett.* **38**, L20303 (2011).
88. Martel, S. J. Progress in understanding sheeting joints over the past two centuries. *J. Struct. Geol.* **94**, 68–86 (2017).
89. Davis, T., Healy, D., Bubeck, A. & Walker, R. Stress concentrations around voids in three dimensions: the roots of failure. *J. Struct. Geol.* **102**, 193–207 (2017).
90. Fernandes, N. F. & Dietrich, W. E. Hillslope evolution by diffusive processes: the timescale for equilibrium adjustments. *Water Resour. Res.* **33**, 1307–1318 (1997).
91. Geyman, E. C., Paige, D. A. & Lamb, M. P. Tectonic uplift, soil production, soil depth, and rock strength at the Dragon's Back Pressure Ridge, Carrizo Plain, California. *Zenodo*. https://doi.org/10.5281/zenodo.12637755 (2024).
92. Brantley, S. L., Goldhaber, M. B. & Ragnarsdottir, K. V. Crossing disciplines and scales to understand the critical zone. *Elements* **3**, 307–314 (2007).

93. Shaanan, U. et al. Progressive fracturing in alluvial clasts. *Geol. Soc. Am. Bull.* **136**, 1097–1110 (2024).
94. Arrowsmith, J. R., Rhodes, D. D. & Pollard, D. D. Morphologic dating of scarps formed by repeated slip events along the San Andreas Fault, Carrizo Plain, California. *J. Geophys. Res. Solid Earth* **103**, 10141–10160 (1998).

Acknowledgements We thank G. Hilley, K. Ferrier and J. West for their feedback and discussions. We also thank H. Alqattan, R. Deng, M. Douglas, S. Houchin, J. Nghiem, J. Reahl, M. Sanders, T. Seeger, K. Thalhammer and O. Wilner for help in the Caltech Ge121 field course. We thank G. Hilley and R. Arrowsmith for sharing details about their previous mapping at the DBPR. Lidar data were provided by the National Center for Airborne Laser Mapping (NCALM) under NSF EAR-0409045. E.C.G. was supported by the NSF Graduate Research Fellowships Program and the Fannie and John Hertz Foundation.

Author contributions E.C.G. and M.P.L. designed the study. D.A.P. advised on the radar acquisition and processing. E.C.G. performed the analysis and wrote the paper, with input from D.A.P. and M.P.L.

Competing interests The authors declare no competing interests.

Additional information

Supplementary information The online version contains supplementary material available at https://doi.org/10.1038/s41586-025-09751-z.

Correspondence and requests for materials should be addressed to Emily C. Geyman.

Peer review information *Nature* thanks Simon Mudd and the other, anonymous, reviewer(s) for their contribution to the peer review of this work. Peer reviewer reports are available.

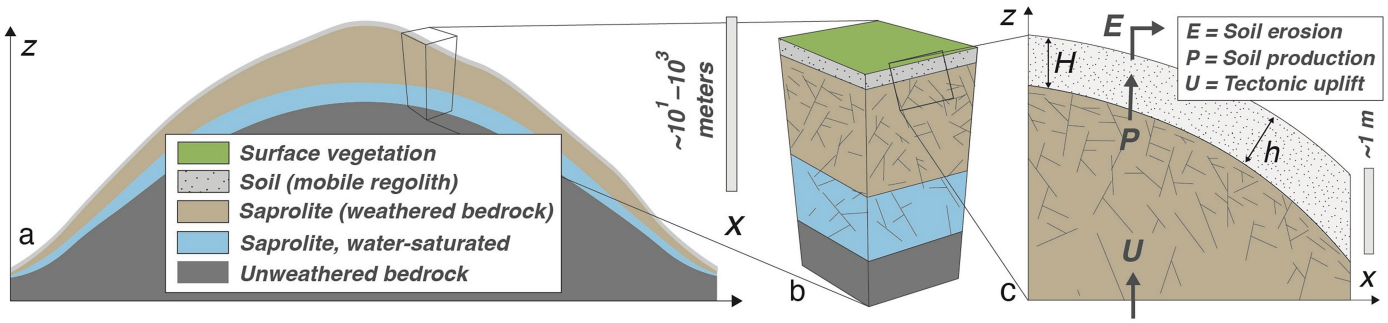

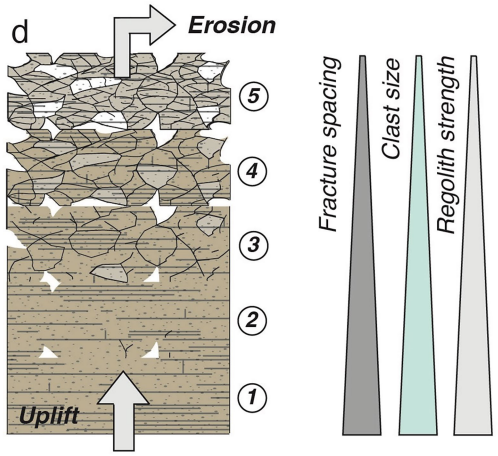

Conceptual model for the time history of a parcel of uplifting rock:

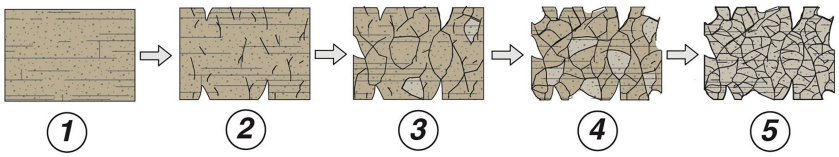

Parent material:
Poorly-lithified siltstone-to-sandstone (Paso Robles Fm.)

Processed regolith:
Parent material is disaggregated to cm-size clasts in a silty-sandy matrix

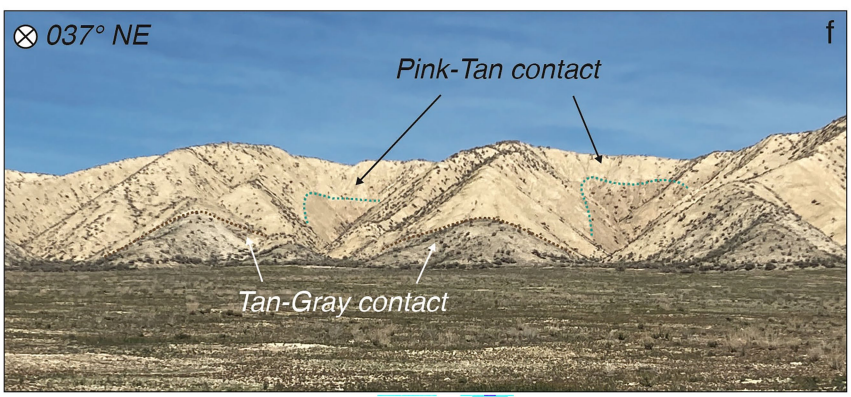

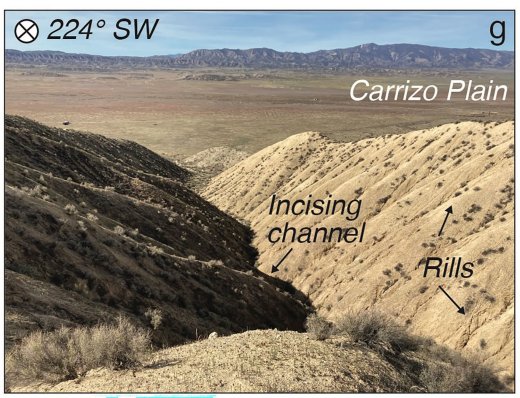

Extended Data Fig. 1 | See next page for caption.

Extended Data Fig. 1 | Soil production and hillslope form at the Dragon's Back Pressure Ridge (DBPR) in the Carrizo Plain, California. (a) An illustration of the transitions from unweathered bedrock to weathered bedrock (saprolite) to the mobile regolith (soil). These sub-surface horizons, in addition to the overlying vegetation canopy, jointly define the 'critical zone'[8,20,68,92]. (a-c) The transition from unweathered to weathered bedrock can occur tens to hundreds of meters beneath the ground surface (a), but the mobile soil layer typically only represents the top 0–2 m[19,21]. (b) With increasing proximity to the surface, the weathered bedrock becomes more fractured[30] and chemically-altered[8,92] until it loses its parent textural composition and disaggregates to individual mobile particles that can move downhill through soil creep, landsliding, etc.[30] (c) The thickness of the soil layer reflects the balance between soil production (*P*) and soil erosion (*E*). Note that the soil thickness can be defined in either the vertical (*H*) or slope-normal (*h*) directions. (d) A conceptual model for the progressive fracturing[93] and break-down[30] of a parcel of uplifting rock at DBPR. (e-g) Field photographs. (e) Perspective shot with the parallel drainages of the DBPR giving way to the flat Carrizo Plain in the foreground and the Temblor Range in the background. The top of the DBPR is marked with a thin dashed white line. At its peak, the DBPR rises approximately 100 m from the surrounding plains[13] (Fig. 4). (f) An illustration of the two stratigraphic contacts visible in eroding hillslopes on the DBPR. The contacts between the Pink and Tan and the Tan and Gray members of the Paso Robles Formation[13,14,56] (Fig. 2) are shown with dotted green and brown lines, respectively. We use the elevations of these stratigraphic contacts to constrain the tectonic uplift at DBPR (Extended Data Figs. 3-4). (g) An example of one of the steep catchments in the middle of DBPR.

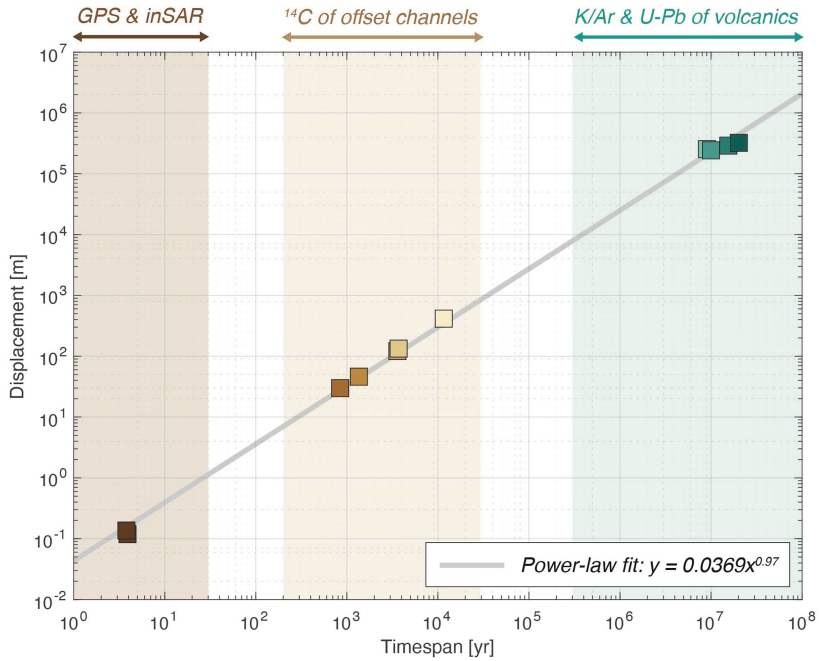

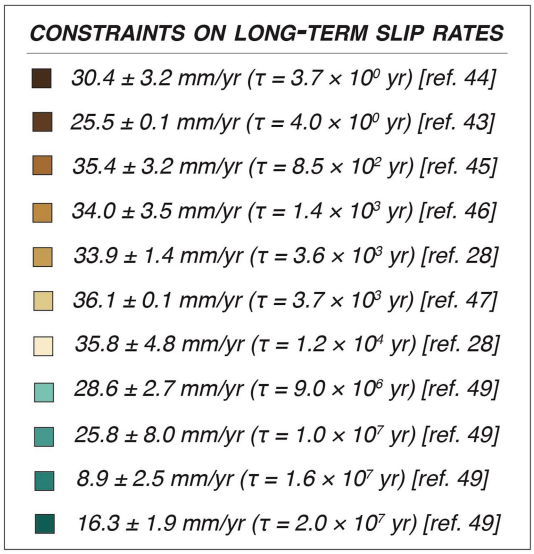

Extended Data Fig. 2 | A compilation of slip rates estimated for the San Andreas Fault in central California on timescales of decades to millions of years[28,43–47,49–54]. On annual to decadal timescales, the fault motion is quantified from GPS and interferometric synthetic aperture radar (inSAR) data[43,44]. On centennial to millennial timescales, fault motion is quantified from offset channels (typically dated with ^{14}C)[28,45–48]. On million-year timescales, fault motion is quantified primarily from radiometrically-dated volcanic rocks and other geological features that are pierced by the fault and have been displaced by approximately 10^1–10^3 km[49–54]. The long-term (million-year-timescale) slip rates compiled by Gooley et al. (2021)[49] are based on piercing points defined by the: (1) granite of the Gabilan Range to the southern Temblor Range Mohnian Santa Margarita conglomerates ($\tau \approx 8.0 - 10.0 \times 10^6$ yrs, $\Delta x \approx 249 - 259$ km)[50–52], (2) granite of the Gabilan Range and Pinnacles volcanic center to the Temblor Range Mohnian Santa Margarita conglomerates ($\tau \approx 6.5 - 13.5 \times 10^6$ yrs, $\Delta x \approx 225 - 260$ km)[50,51], (3) Relizian–Luisian basinal facies of the Monterey Formation ($\tau \approx 13.5 - 17.5 \times 10^6$ yrs, $\Delta x \approx 260 - 320$ km)[54], and (4) Saucesian paleobathymetry ($\tau \approx 17.5 - 22.9 \times 10^6$ yrs, $\Delta x \approx 320 - 325$ km)[53].

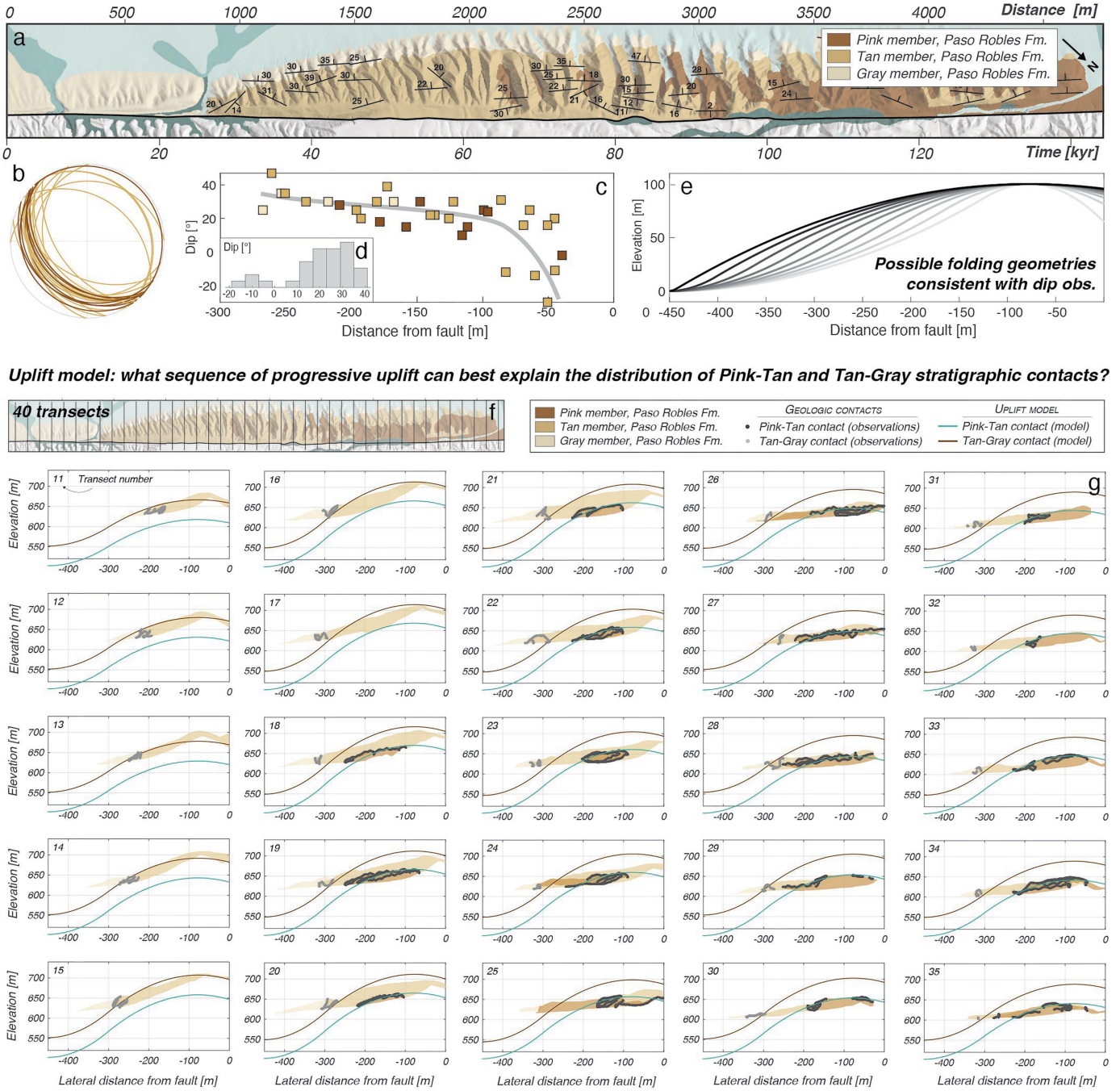

Extended Data Fig. 3 | An illustration of the tectonic uplift model, constrained using the positions and elevations of the three units of the Paso Robles Formation. (a) Bedding plane orientations, measured by Arrowsmith (1995)[14], show that sedimentary layers in the Paso Robles Formation adopt an approximately monoclinal folding geometry at DBPR, whereby beds that are more distal from the San Andreas Fault (SAF) are dipping to the southwest at angles of approximately 30°, and beds that are proximal to the SAF are flat-lying or dipping slightly to the northeast. The basemap in (a) is the geological map of Arrowsmith (1995)[14], modified in this study using field observations and high-resolution RGB imagery made available by the National Agriculture Imagery Program (NAIP). (b) Stereonet showing bedding plane orientations across DBPR, colored by stratigraphic unit. (c) Dip angle as a function of the distance from the SAF. Dip angles are defined as positive to the southwest. (d) A histogram of all dip angles. (e) A range of possible folding geometries used in the uplift model (Fig. 2). (f-g) An illustration of the data used to constrain the uplift model. (f) We divide the DBPR into 40 equally-spaced segments, which is the maximum number of segments that can be generated where each segment includes at least one drainage divide (ridgeline) and one trunk channel, meaning that each segment samples the local elevation maxima and minima for that distance along DBPR. (g) Within each segment, we extract the elevation and position (lateral distance from SAF) of every 1 m^2 in the lidar digital elevation model (Fig. 2a), coded by the stratigraphic unit from the geological map of Arrowsmith (1995)[14] (the Pink, Tan, or Gray Member of the Paso Robles Formation). We also extract the position and elevation of all geological contacts (Pink–Tan and Tan–Gray contacts). Our uplift model seeks to best capture the geological observations, which means that all surface exposures of the Gray Member should lie above our inferred Tan–Gray contact, all surface exposures of the Tan Member should occur between our inferred Pink–Tan and Tan–Gray contacts, and all surface exposures of the Pink Member should lie below our inferred Pink–Tan contact.

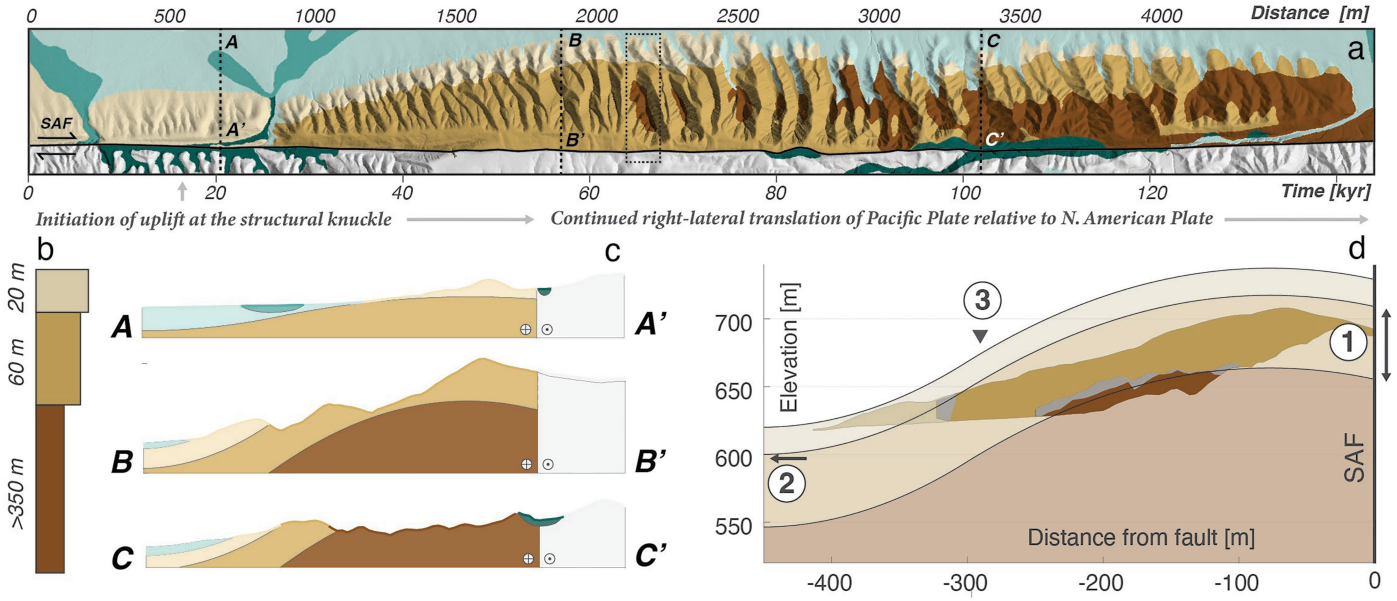

Extended Data Fig. 4 | An illustration of the model parameters and sources of uncertainty in our Markov Chain Monte Carlo (MCMC) inversion for the uplift history (see Fig. 2). (a-c) The core observation underlying the model for tectonic uplift at DBPR is the fact that the initially flat-lying Pink, Tan, and Gray Members of the Paso Robles Formation are progressively exposed at the surface at DBPR. (c) This exposure reflects a combination of tectonic uplift ('rock uplift' as defined by England & Molnar[36]) and subsequent erosion (denudation). By tracking the elevations of the different geologic units, we can isolate the component of rock uplift. (d) Our uplift model fits a simple monoclinal folding geometry to the geological observations (Extended Data Fig. 3). This model assumes that there is no uplift at a distance of 450 m from the San Andreas Fault, consistent with our observations (Extended Data Fig. 5). There are three free parameters in our uplift model: ① the stratigraphic thickness of the Tan Member (e), ② the initial position (distal elevation) of the contact between the Tan and Gray Members (f), and ③ the position of the fold inflection (g), which defines the folding geometry as shown in Extended Data Fig. 3e. (h-j) A simple gridded search illustrates the tradeoffs between the three model parameters in (e-g). (h) The loss function ('normalized error') reflects how well the simulated uplift (Fig. 2) explains the two types of geological observations we have at DBPR: (1) the elevations of stratigraphic units, and (2) the dip angles and orientations of bedding planes. For our final uplift model (Fig. 2), rather than performing a gridded search as shown in (i-j), we perform an MCMC inversion, allowing each model parameter to explore a range of values informed by the distributions shown in (e-g).

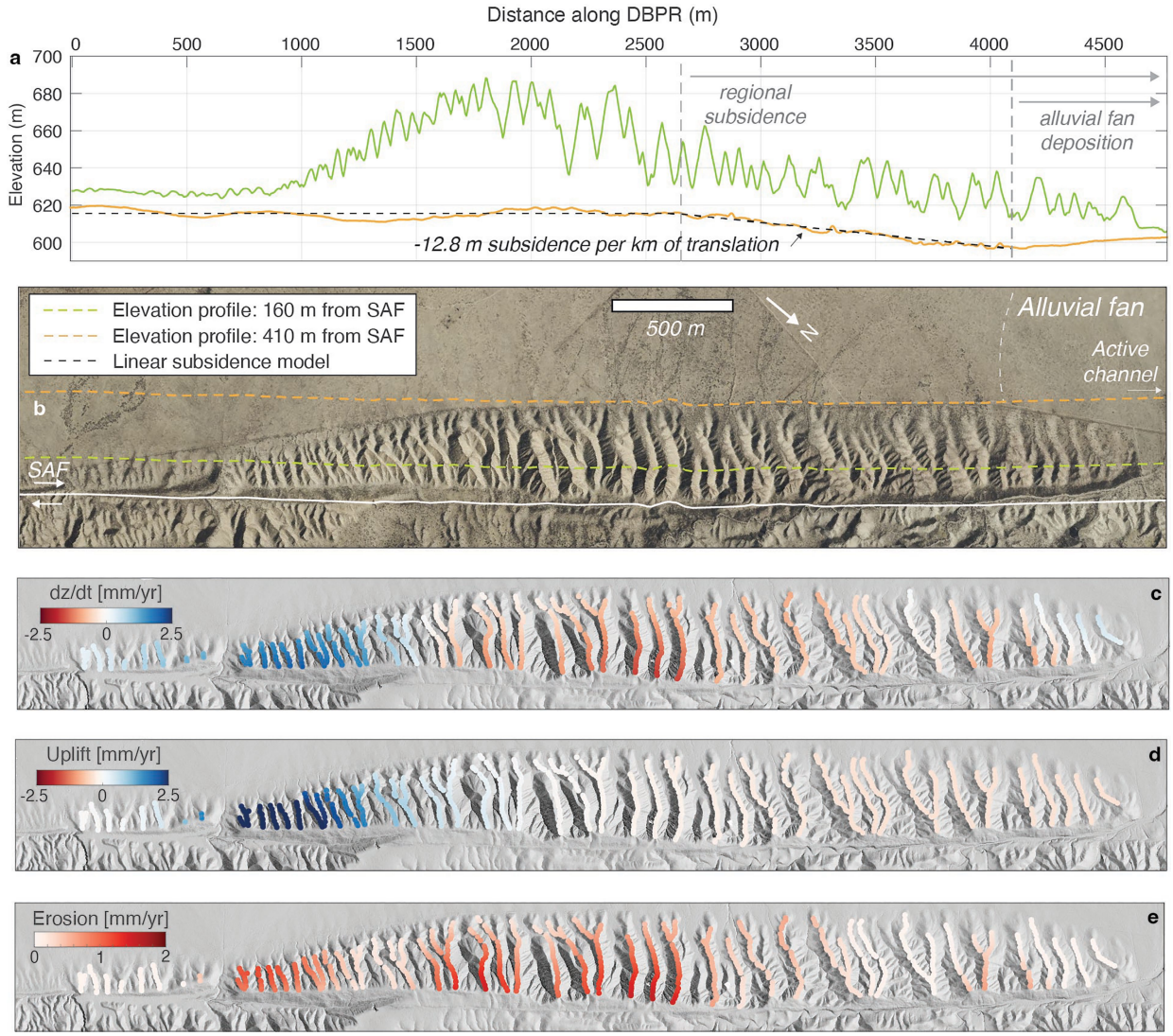

Extended Data Fig. 5 | Quantifying uplift vs. subsidence and partitioning surface elevation change into the components from tectonic uplift and erosion. (a-b) Identifying a small amount of regional subsidence at DBPR. (a) Elevation profiles proximal and distal to the San Andreas Fault (160 m and 410 m away, respectively). Note that, at the zone of maximum uplift (~1000–2000 m along DBPR), the SAF-proximal elevation rises by approximately 60 m, with just 0–3 m of elevation change at the distal transect. However, starting at a distance of around 2700 m along DBPR, the distal elevation drops from the roughly constant value of 615 m to a minimum of 596 m. This approximately linear pattern of decreasing elevation corresponds to ~12.8 m of subsidence per kilometer of lateral translation, or, assuming a horizontal slip rate[28] of 33 mm/yr, a subsidence rate of 0.39 mm/yr. In the distance range of 4100–4500 m along DBPR, the distal elevation rises. However, this elevation increase coincides with the intersection of the distal elevation transect with Quaternary alluvial fan deposits[14] (b), so we believe it is unlikely that the rise in elevation represents renewed uplift. (c) We use a space-for-time substitution to estimate $\frac{dz}{dt}$ between adjacent ridgelines at DBPR. Specifically, we fit a surface to the lidar-measured ridgeline elevations. Next, we compute the lateral translation distance between adjacent ridgelines. Finally, we assume a long-term slip rate[13,28] along the SAF of 33 mm/yr (Extended Data Fig. 2) to translate the ridge-to-ridge spacing into an estimate of temporal duration. (d) The uplift model in Fig. 2, based on stratigraphic and structural observations of the Paso Robles Formation, constrains the uplift rate (U). (e) The ridgetop erosion rate is the difference between the uplift term (d) and the observed rate of surface elevation change (c).

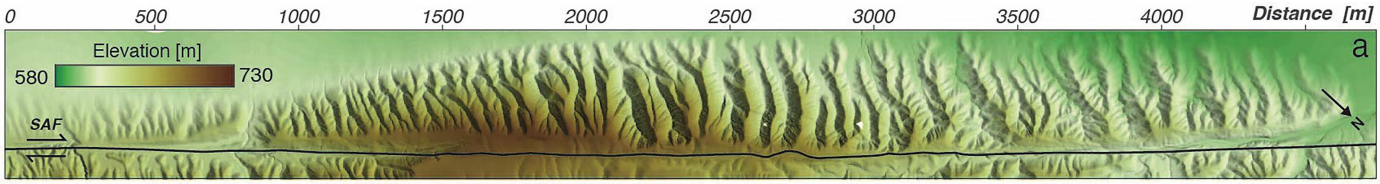

Field measurements: ground-penetrating radar (GPR) surveys, cone penetrometer stations, and soil pits

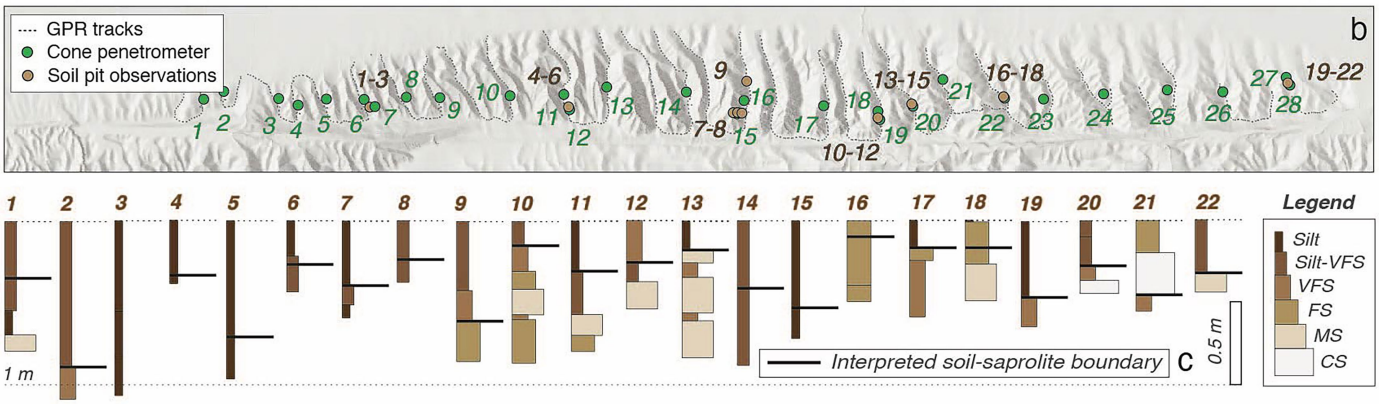

Calibration & validation of GPR-based soil thickness: paired GPR & cone penetrometer measurements

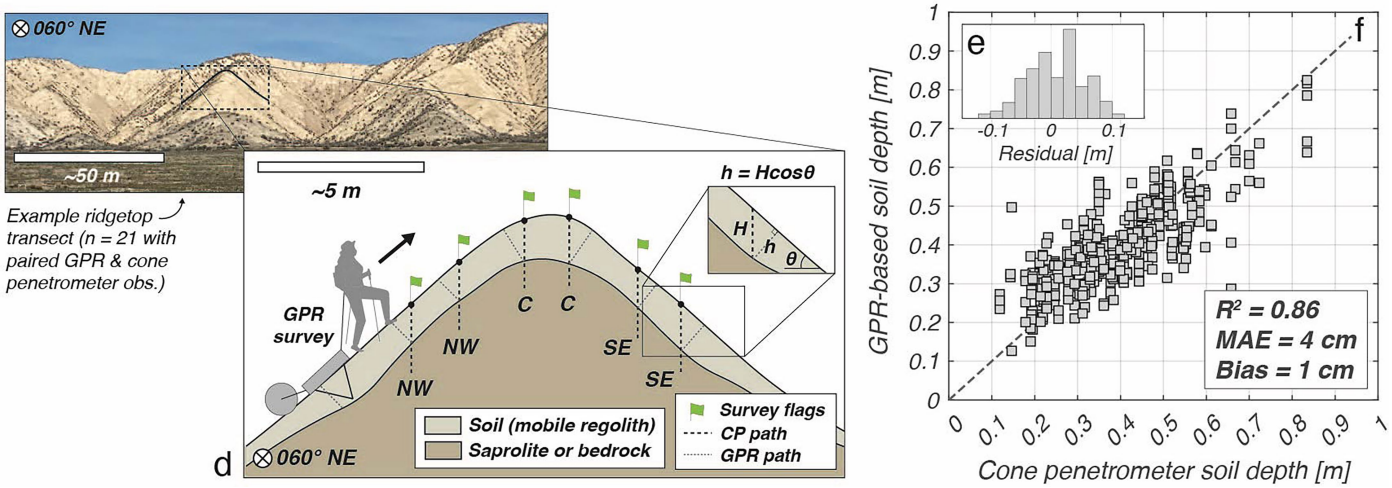

Extended Data Fig. 6 | Field observations from the Dragon's Back Pressure Ridge (DBPR). (a) Lidar topography of the DBPR and the San Andreas Fault (SAF)[55]. The zone of the maximum tectonic uplift rate is centered around a distance of 1000 m along DBPR[13]. (b) Locations of field observations (GPR profiles, cone penetrometer measurements, and hand-dug soil pits). Labels for the cone penetrometer transects are written in green and labels for the soil pits are written in brown. (c) Stratigraphic columns logged at the 22 soil pit locations. The horizontal black line shows the inferred position of the soil–saprolite boundary, and the box width and color indicates the predominant grain size of the sediments. Note that the bedrock at this field site is the Pliocene-Pleistocene Paso Robles Formation[94], which consists of siltstones, sandstones, and conglomerates. In the legend in (c), VFS = very fine sand, FS = fine sand, MS = medium sand, and CS = coarse sand. (d) An illustration of the field methodology for collecting paired cone-penetrometer and GPR observations. At 28 ridgetop locations along the length of DBPR (b), we marked short (10–15 meter) transects perpendicular to the ridge axis with a measuring tape. We collected cone-penetrometer measurements (see Extended Data Fig. 7) at six or more locations along each transect: 2 stations on the northwest (NW) side of the ridge, 2 stations on the central (C) part of the ridge, and 2 stations on the southeast (SE) side of the ridge. We marked each station with a survey flag, and then acquired a GPR profile along the same transect, marking the position of each flag in the survey metadata. Note that the cone penetrometer measurements probe the soil layer vertically (in the direction of gravity), whereas the radar observations image the soil perpendicular to the local surface slope. The soil thicknesses in the vertical (H) and slope-normal (h) directions are linked as $h = H\cos\theta$. (e-f) A comparison of co-located cone penetrometer and GPR-based estimates of soil thickness. Panel (e) shows a histogram of residuals from the regression in (f). The residuals are roughly normally-distributed and centered around 0.0 m. In (f), the R^2 value is 0.86, the mean absolute error (MAE) is 0.04 m, and the bias (average residual of predicted minus ground-truth) is 0.01 m.

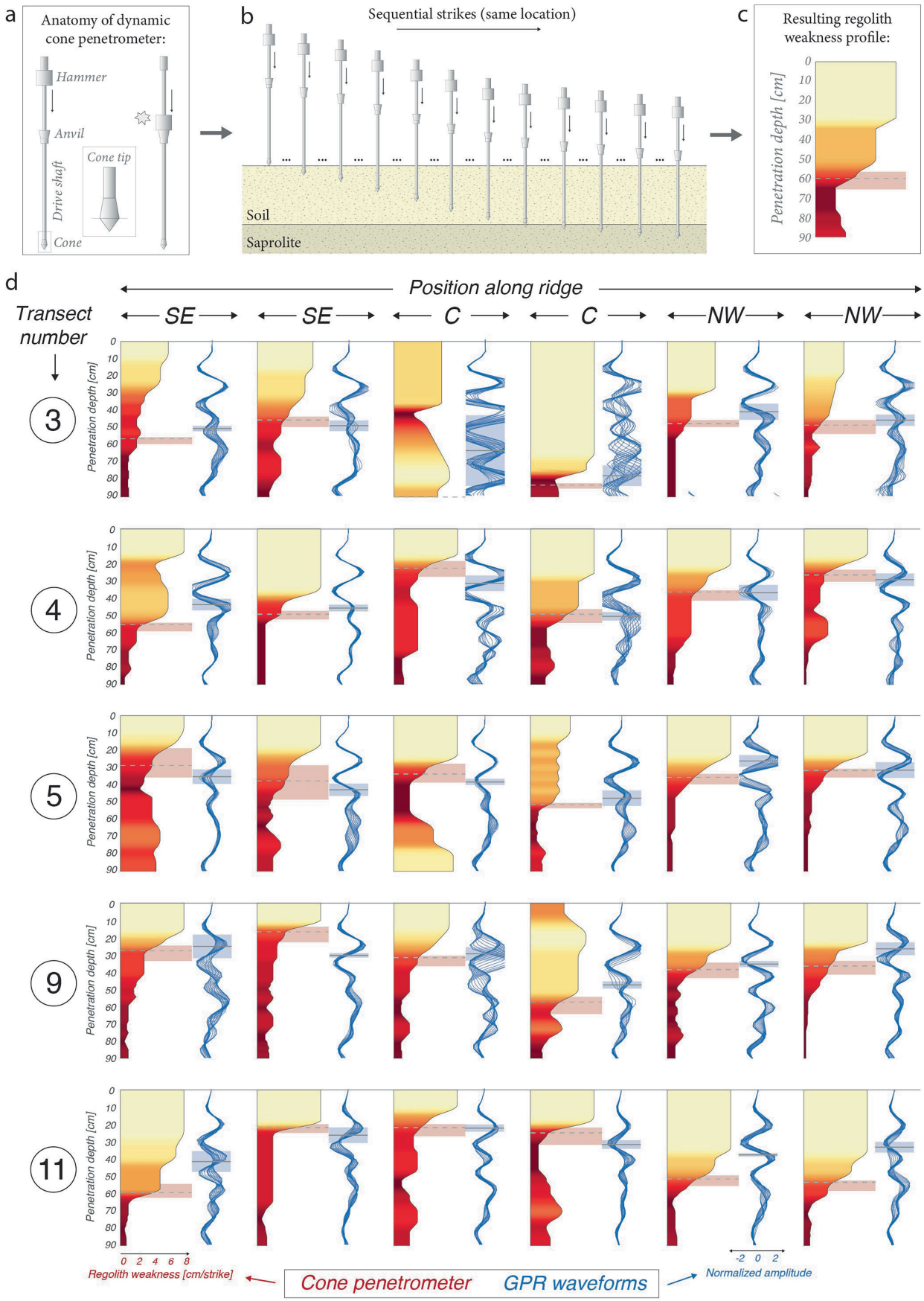

Extended Data Fig. 7 | See next page for caption.

Extended Data Fig. 7 | Observations from the hand-driven dynamic cone penetrometer. (a-c) Basic anatomy of the cone penetrometer (a), and an illustration of how the cone penetrometer is used to extract regolith strength profiles (b-c). The cone penetrometer has a conical tip that penetrates deeper into the subsurface each time the falling weight is dropped onto the fixed anvil located at the top of the driving rod. The raw data collected at each of the $n = 212$ cone penetrometer profiles (see Extended Data Fig. 6b for the site locations) is the cumulative penetration depth as a function of the cumulative number of strikes (the number of times the hammer was dropped). We take the numerical derivative of these cumulative strikes vs. penetration depth observations to calculate the local (depth-dependent) regolith weakness, reported in units of cm of penetration per strike. (d) A comparison between the cone penetrometer observations of regolith weakness and the co-located power-corrected GPR waveforms (see Supplementary Information). Five ridge-top cross-sections are illustrated here. Another five example transects are shown in Fig. S7 of the Supplementary Information. Shaded red boxes show the estimated position of the soil–saprolite boundary based on the cone penetrometer observations, and shaded blue boxes show the estimated position of the soil–saprolite boundary based on the GPR observations. A comparison between the co-located cone penetrometer and GPR-based estimates of soil thickness is shown in Extended Data Fig. 6f.

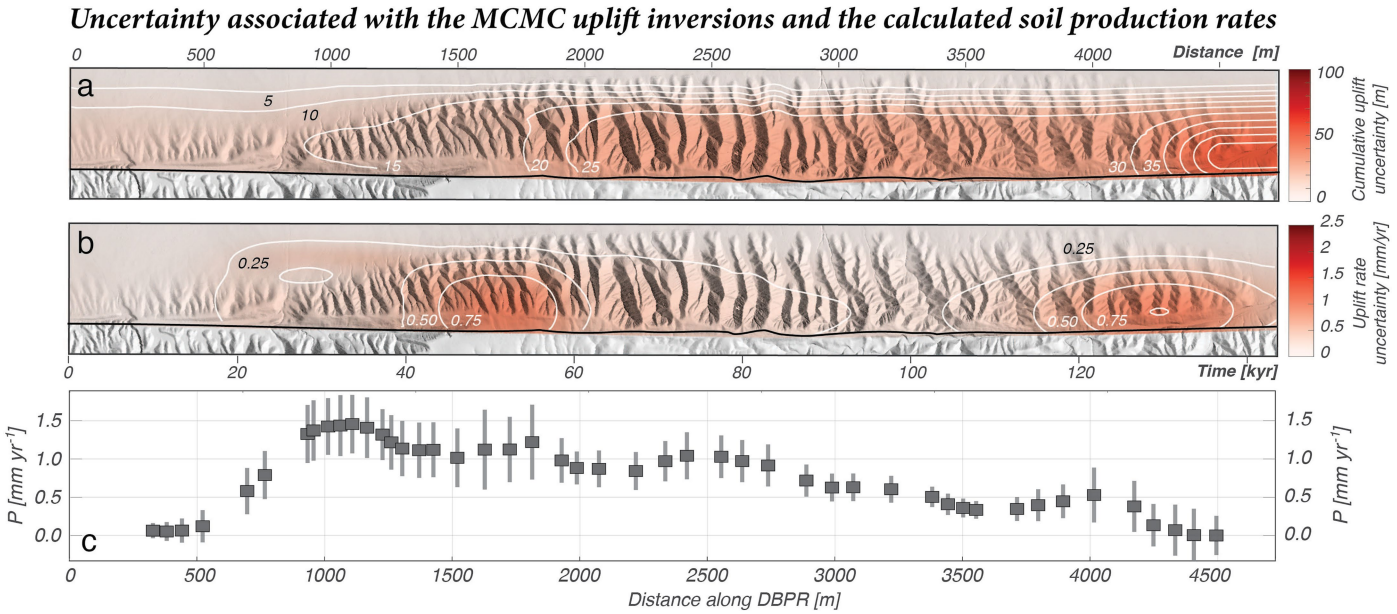

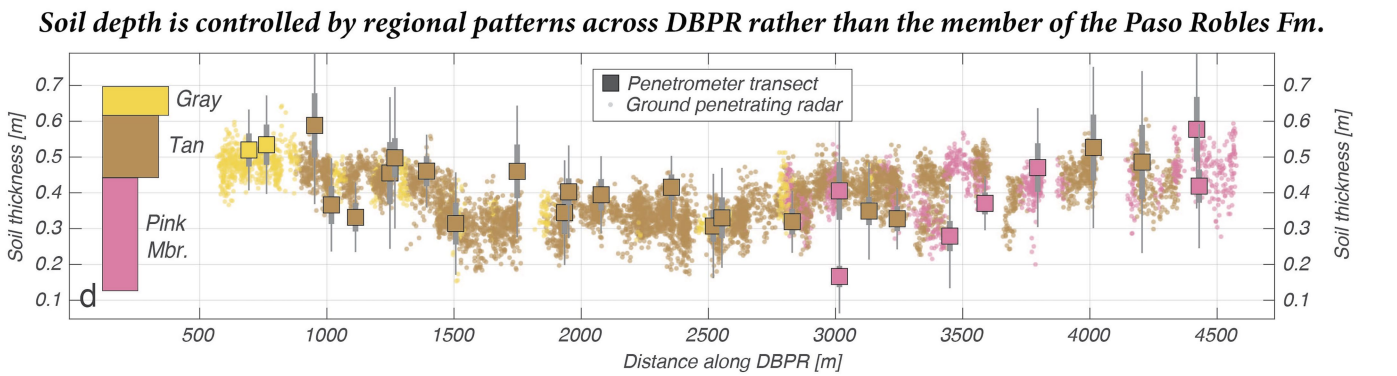

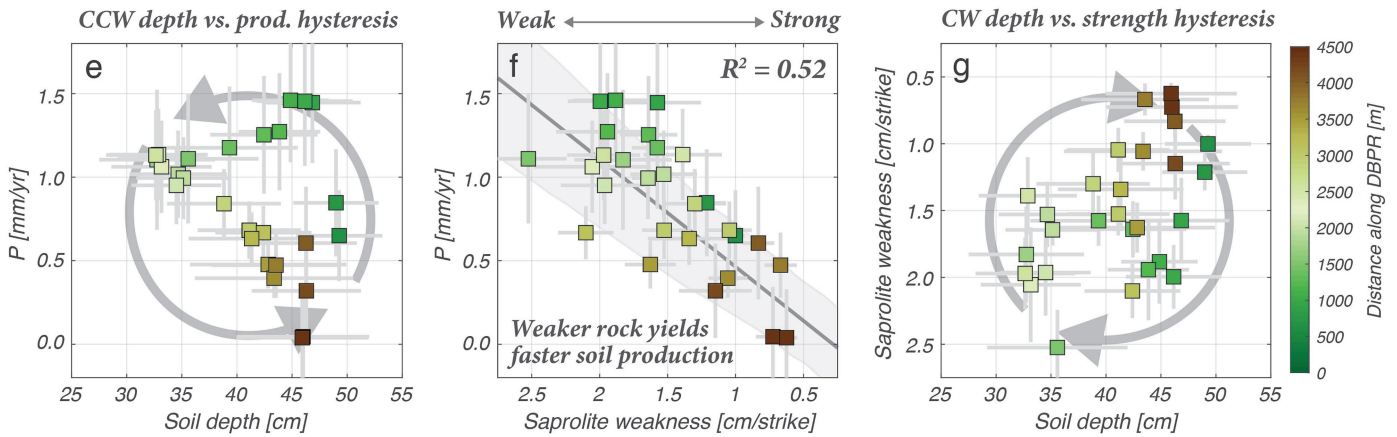

Extended Data Fig. 8 | See next page for caption.

Extended Data Fig. 8 | Sensitivity tests. Panels (a-c) show an evaluation of the uncertainty associated with the uplift and soil production estimates, panel (d) shows an analysis of whether trends in soil thickness are controlled by the bedrock lithology, and panels (e-g) show a test of whether the observations in Fig. 5 are robust to different soil thickness datasets. (a-b) Spatial patterns of uncertainty in the cumulative uplift (a) and uplift rate (b) from the MCMC uplift inversions illustrated in Fig. 2. In (a)-(b), the contours and the shaded red colors show the interquartile range (25th to 75th percentiles) of the MCMC uplift estimates. Typical uncertainties on the local uplift rate are approximately 0.25 mm/yr. Note that the second zone of high uncertainty in the reconstructed uplift rates (at a distance of approximately 4000 m along DBPR) corresponds to the ambiguous and poorly-constrained termination of the slow regional subsidence illustrated in Extended Data Fig. 5a-b. The tectonic motion in this terminal region of the DBPR is more poorly constrained because there is no longer an exposed stratigraphic contact between the Tan and Gray members of the Paso Robles Formation (see the geological map in Fig. 2). (c) Reconstructed soil production rates (via equation (2)), with associated 1σ uncertainties. The P values are estimated for each of the 47 ridgelines shown in Extended Data Fig. 6, using interpolated soil thickness data from (d) to estimate the $\frac{dH}{dx}$ term at ridgelines with no soil thickness measurements. (d) A comparison between the soil thickness estimates made from the cone penetrometer transects and the GPR profiles, both plotted as a function of distance along DBPR. Soil thickness observations are color-coded according to the stratigraphic unit in the Paso Robles Formation. We do not find evidence that the soils above the closely-spaced Gray, Tan, or Pink members are systematically thinner or thicker. (e-g) Same crossplots as in Fig. 5, but here the soil thickness data are based on the GPR measurements rather than the in-situ cone penetrometer observations. Comparison of this figure with Fig. 5 shows that both soil thickness datasets reproduce the key observation of our study: there is a counter-clockwise (CCW) hysteresis of soil thickness vs. soil production rate (e), and a clockwise (CW) hysteresis of soil thickness vs. saprolite strength (g).

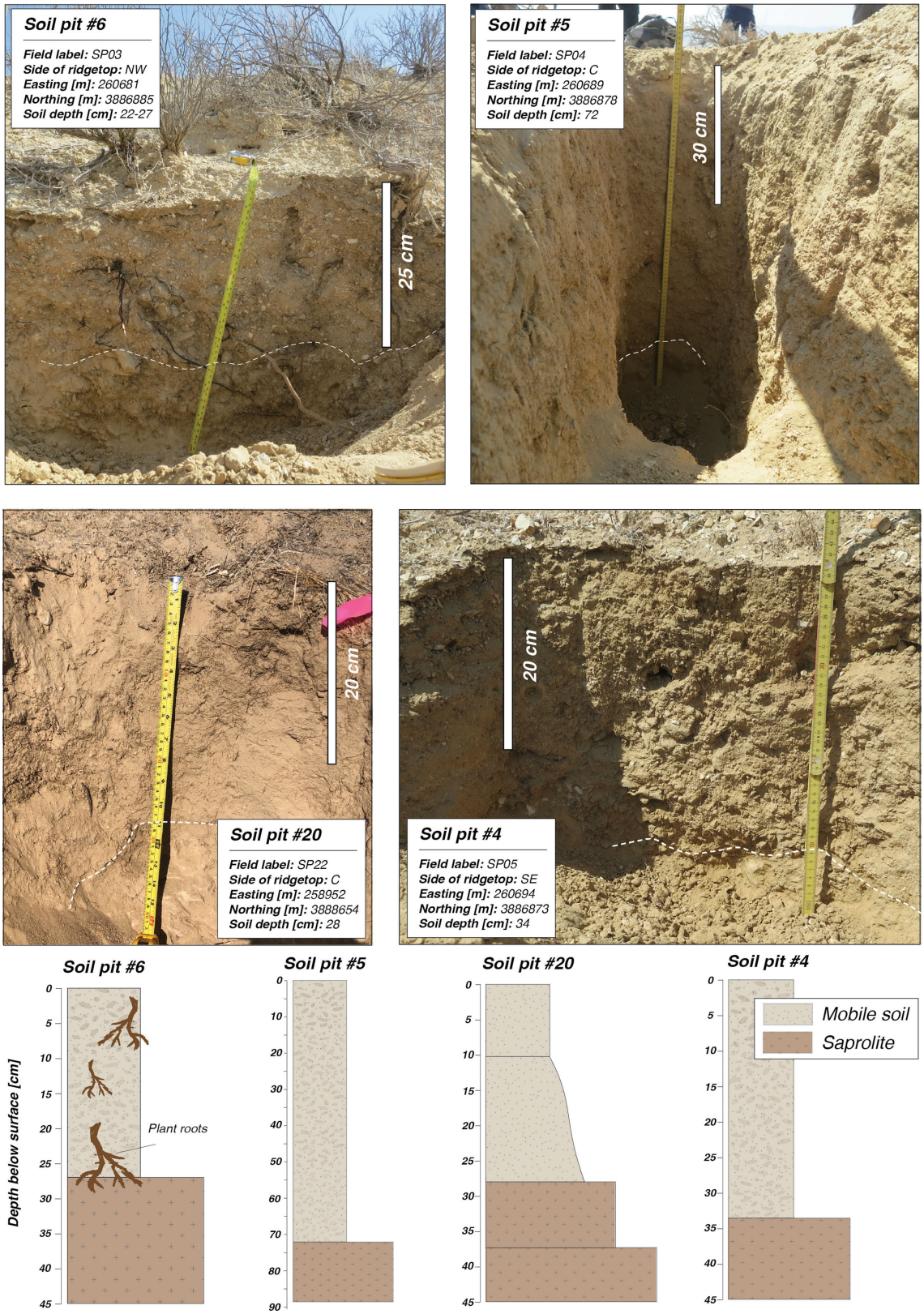

Extended Data Fig. 9 | Example soil pit observations. In total, we dug $n = 22$ soil pits along the length of DBPR (see Extended Data Fig. 6c). At each soil pit, we documented vertical changes in: (i) the grain size of the sedimentary matrix, (ii) the composition, angularity, size, and abundance of clasts, (iii) the degree of cementation or lithification, and (iv) the preservation or destruction of the primary fabric of the sedimentary rocks of the Paso Robles Formation. We used these textural observations to infer the position of the soil–saprolite boundary. See Figs. S14-S18 of the Supplementary Information for additional observations.

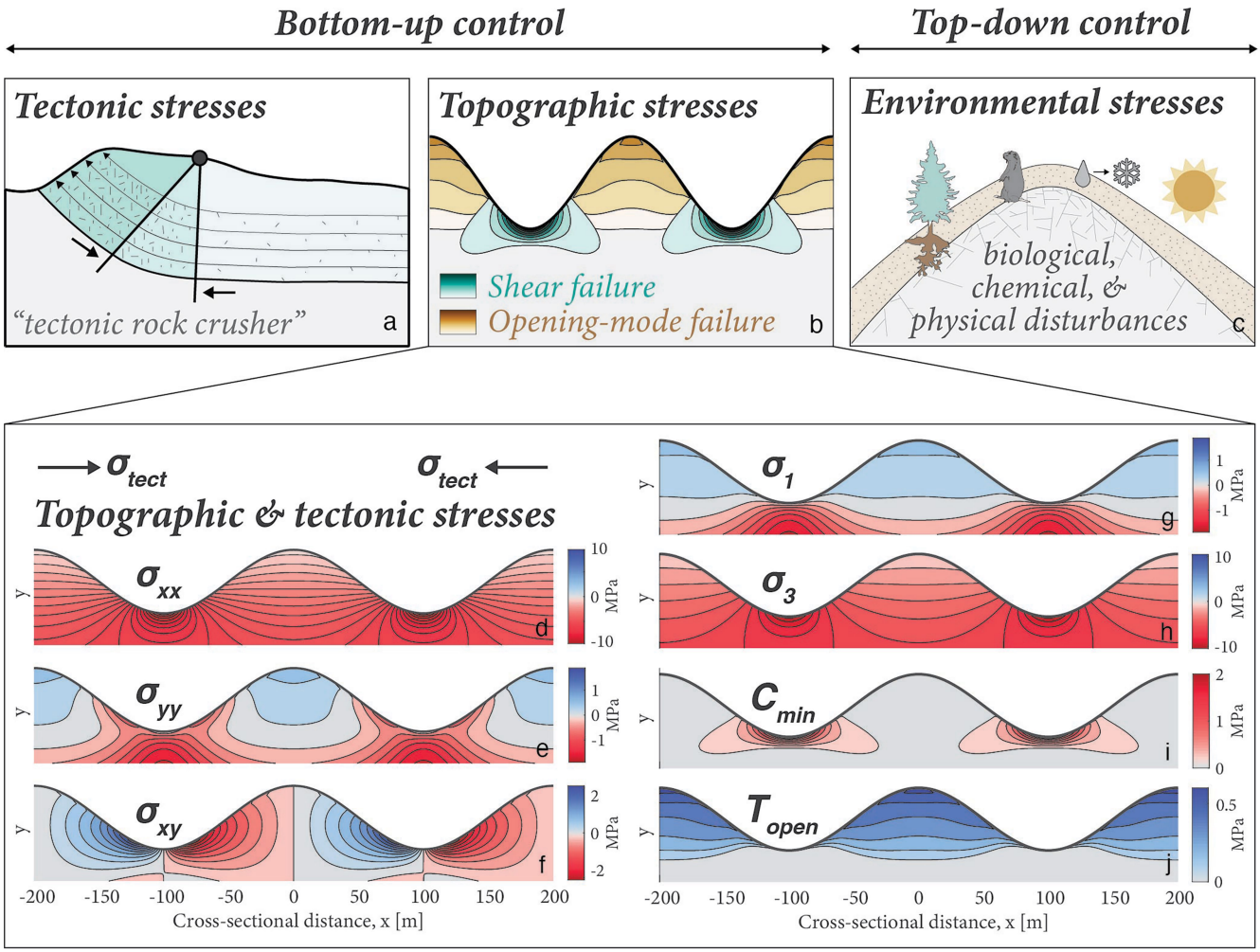

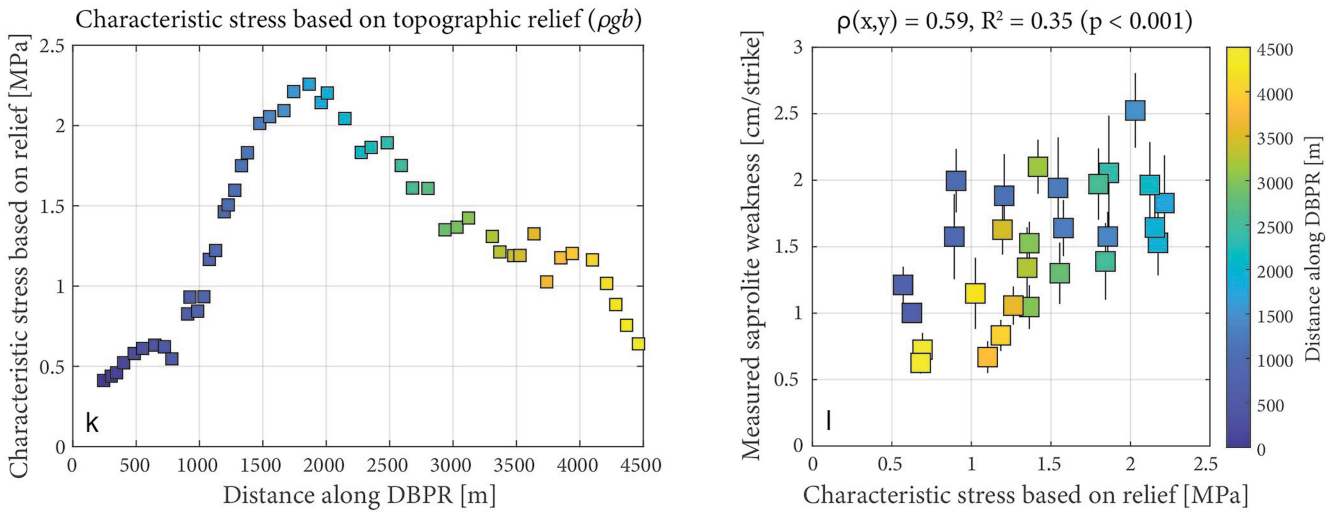

Extended Data Fig. 10 | See next page for caption.

Extended Data Fig. 10 | A bottom-up control on soil production through rock fracture. (a-c) A conceptual model in whuich three broad categories of stress influence rock strength and thereby regulate the breakdown of saprolite to mobile soil: (a) tectonic stresses, (b) topographic stresses, and (c) environmental stresses. (a) First, tectonically-active convergent settings must undergo substantial strain[67,80,81], which, in the brittle part of the crust, results in rock fracture[67]. Thus, tectonically-active uplifting regions will have more highly-fractured rock[65,67] supporting faster soil production[65,75,78]. (b) Second, as shown by refs. 27,83,84, the topography itself can become a fracture-forming agent[27]. (c) Third, environmental stresses, including cyclical temperature variations and biological factors (e.g., tree root expansion) are near-surface stresses that also are capable of fracturing rock[30]. The conceptual models for (a) and (c) come from ref. 67 and ref. 75, respectively. (d-j) Numerical exploration of topographic stresses at DBPR, based on the boundary-element code from ref. 89. The topography in (d-j) is shown with no vertical exaggeration. In the simulations shown in (d-j), the applied regional tectonic stress, σ_{tect}, is -5.2 MPa. (d-f) Estimates of stresses in the orientations σ_{xx}, σ_{yy}, and σ_{xy}. (g-h) Principal stresses σ_1 and σ_3, derived from (d-f). Estimates of the propensity for forming shear (mode II) fractures (i) and opening (mode I) fractures (j). (i) Following ref. 85, C_{min} [MPa] is the minimum cohesion required to prevent shear fracture. (j) Following refs. 86,87, T_{open} [MPa] is the tensile stress driving opening-mode fractures. Note that rock fracture need not occur through critical failure, as expressed with a Mohr-Coulomb framework. Rather, fracture can occur through the process of subcritical cracking[30], which proceeds at stress intensities much lower than the critical stress intensity (K_c). Subcritical cracking proceeds slowly, but meaningfully over the approximately 10^5-yr timescales that rocks spend in the critical zone[30]. (k-l) A simple empirical test of whether topographic stresses could be responsible for weakening the saprolite at DBPR. Following refs. 27,84, we define the characteristic stress generated from topographic relief as $\rho g b$, where ρ is the density of rock [kg m^{-3}], g is the gravitational acceleration [m s^{-2}], and b is the ridge-to-valley relief [m]. (k) Using the basin relief in Fig. 4b (and assuming a bulk density of $\rho = 2{,}317$ kg m^{-3})[39], we constrain the pattern of the characteristic stress at DBPR[84] and compare the result to the measured saprolite weakness (Fig. 4c). (l) The characteristic stress and saprolite weakness are significantly and positively correlated, with a Pearson correlation coefficient $\rho(x, y) = 0.59$ ($p < 0.001$).